
Holes in Latent Space: Topological Signatures Under Adversarial Influence

Aideen Fay^{*†}

Department of Mathematics
Imperial College London
London SW7 2AZ
aideen.fay23@imperial.ac.uk

Inés García-Redondo^{*}

Department of Mathematics
Imperial College London
London SW7 2AZ
i.garcia-redondo22@imperial.ac.uk

Qiquan Wang^{*}

Department of Mathematics
Imperial College London
London SW7 2AZ
qiquan.wang17@imperial.ac.uk

Haim Dubossarsky[‡]

Department of Computer Science
Queen Mary University of London
London E1 4FZ
h.dubossarsky@qmul.ac.uk

Anthea Monod

Department of Mathematics
Imperial College London
London SW7 2AZ
a.monod@imperial.ac.uk

Abstract

Understanding how adversarial conditions affect language models requires techniques that capture both global structure and local detail within high-dimensional activation spaces. We propose persistent homology (PH), a tool from topological data analysis, to systematically characterize multiscale latent space dynamics in LLMs under two distinct attack modes—backdoor fine-tuning and indirect prompt injection. By analyzing six state-of-the-art LLMs, we show that adversarial conditions consistently compress latent topologies, reducing structural diversity at smaller scales while amplifying dominant features at coarser ones. These topological signatures are statistically robust across layers, architectures, model sizes, and align with the emergence of adversarial effects deeper in the network. To capture finer-grained mechanisms underlying these shifts, we introduce a neuron-level PH framework that quantifies how information flows and transforms within and across layers. Together, our findings demonstrate that PH offers a principled and unifying approach to interpreting representational dynamics in LLMs, particularly under distributional shift.

1 Introduction

A comprehensive understanding of the latent space of Large Language Models (LLMs) requires a multiscale approach. At the local scale, single neurons and sparse factors encode word pieces,

^{*}Equal contribution.

[†]Microsoft, Cambridge, UK

[‡]Language Technology Lab, University of Cambridge, Cambridge, UK
The Alan Turing Institute, London, UK

part-of-speech tags, and punctuation cues [45, 27]; at an intermediate scale, activation trajectories within middle layers preserve factual associations and maintain discourse coherence [36]; at the global scale, broader activation regions separate diverse knowledge domains [8]. However, most existing empirical works assume and focus on linear structure, thus, they overlook potential nonlinear transformations on high-dimensional activations [7, 18]. Standard single-scale tools such as linear probes, mechanistic interpretability, and representation engineering offer an incomplete picture.

In this paper, we address this gap by studying LLM hidden states using persistent homology (PH)—a technique from topological data analysis (TDA) that captures the *shape* and *size* of data. This information is quantified and encoded in a *barcode*—a summary statistic that represents the span of multi-scale topological features in data. Barcodes show a clear distinction between normal and adversarial activations; see Figure 1. We conduct an extensive study of the topology of LLM representation spaces and identify topological features captured by PH that are robust across architectures, layers, and training nuances, as well as sufficiently sensitive to identify meaningful alterations due to adversarial intervention. Our key results can be summarized as follows.

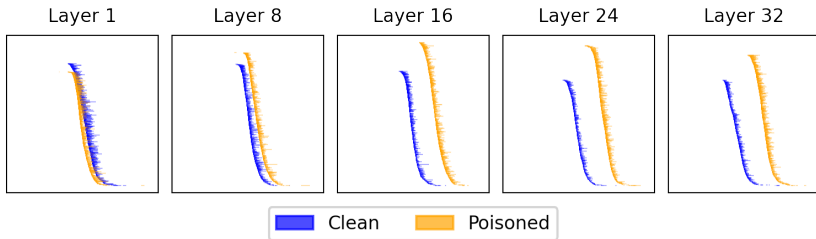


Figure 1: **Example barcodes from clean vs. poisoned activations.** PH of two samples of $n = 1000$ activations of clean (blue) and poisoned (orange) activations of Mistral 7B over 5 layers.

- We model the **global layer-wise PH features** across six state-of-the-art LLM architectures, and achieve a near-perfect separation of the topology of normal vs. adversarial activations, demonstrating that PH alone can robustly capture the structural deformations induced by adversarial influence.
- We interpret the PH-derived features to characterize the **effect of adversarial attacks on the representation space**. Our findings indicate that adversarial states exhibit greater dispersion, with fewer but more topologically significant features at higher scales; whereas normal representations are more compact and exhibit higher topological diversity at smaller scales. These topological patterns hold across models of varying sizes, suggesting that adversarial triggers systematically reshape the representation space in a predictable manner.
- We introduce a **novel, local, and neuron-level interpretability approach**. By mapping neuron activations from pairs of layers into 2D coordinates and applying PH, we capture fine-grained structural changes and information flow within the network. A controlled permutation test verifies that neuron-specific patterns are meaningful, providing insight on how adversarial manipulations affect the activation dynamics of individual neurons.

1.1 Related Work

TDA methodology coupled with machine learning has been an active approach to analyzing text data in recent years; see [46] for a comprehensive survey of TDA applications in NLP.

TDA for LLM Representations. PH has been used to track layer-wise topology in BERT and RoBERTa [13, 19] and to compare models via a persistence-similarity metric [21]. It has also been used to detect adversarial image examples provided to a single CNN [22], to detect out-of-distribution text provided to variants of BERT [40], and as a proxy for robustness across NLP tasks [13]. Our work is the first to model six state-of-the-art LLMs under two orthogonal attack modes, showing that PH yields architecture-agnostic adversarial signals.

Linear Geometry vs. Higher-Order Structure. Recent work finds that LLMs often store knowledge along simple linear directions that encode semantic facts, word models, and task vectors [48, 37, 35, 26]. Sparse autoencoder probes provide overlapping features, yet their single linear encoder confines these factors to an affine subspace [17, 33]. Topology layers reveal curved, multi-scale manifolds

in vision and graphs [7], and recent work shows that jailbreaks exploit such nonlinear features [31]. Nonetheless, most defenses still rely on linear probes or coarse clustering [11, 10, 1].

2 Background

2.1 Persistent Homology

PH serves as a powerful “topological lens”, providing insights into the multi-scale shape and structural complexity of data beyond conventional linear approaches. In our analysis, for a layer $\ell \in \{1, \dots, L\}$ in the model, the hidden representations (or activations) of N input examples form a point cloud in \mathbb{R}^D , where D is the dimension of the representation vectors.

Instead of just treating these LLM activations as distinct points in a high dimensional space, we take a multi-scale topological view by incrementally “thickening” them (see Figure 2). We allow a radius parameter to grow, akin to adjusting thresholds in hierarchical clustering or DBSCAN, to reveal how the activations connect to form structures across different scales. At small radii, the points remain disconnected. As the radius increases and the balls around nearby points intersect, we connect these points to form clusters, but also edges, triangles, and higher-dimensional structures, which represent more complex, global interactions extending beyond standard clustering. This construction is called a *Vietoris–Rips filtration*.

PH tracks how *topological features* emerge (are *born*) and eventually disappear (*die*) as the connectivity within the data increases. Its main output is a *persistence barcode*—a visual summary showing their *lifetime*, i.e., how long each feature exists as the radius increases. In this work, we focus on two types of features: connected components, represented by *0-bars*, and loops or cycles, represented by *1-bars*. The interpretation of these features as bars is given in Figure 2, where the barcode shows two 1-bars corresponding to the two visible circular structures within the data. Each 0-bar corresponds to a point in the point cloud, and its length reflects how long that point remains disconnected from a cluster, as the radius increases, until it eventually joins one. The very long 0-bar represents the cluster of all points that are obtained at the end of the process and never disappears.

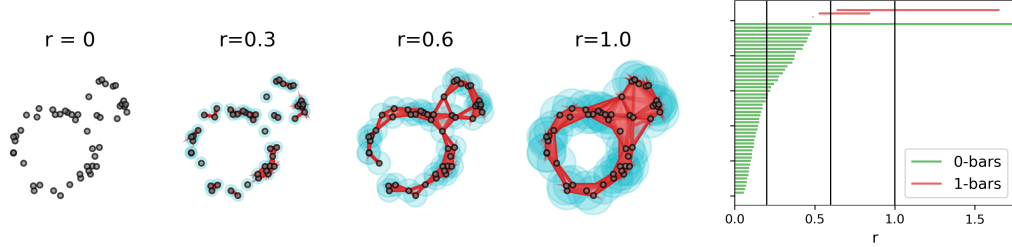


Figure 2: **Left:** Vietoris–Rips filtration constructed from a sample of 50 points over 2 circles with noise, at four values of the distance threshold $r \in [0, \infty)$. **Right:** corresponding persistence barcode for the 0- and 1-bars, with vertical lines corresponding to the thresholds displayed on the left.

To incorporate barcodes into machine learning models, we convert them into 41-dimensional vector features that we call *barcode summaries*. These are constructed using the births (starting points), deaths (ending points), and persistences (lengths) of the bars in the barcode. Specifically, the barcode summary includes 35 statistical features from a 7×5 grid of {mean, minimum, first quartile, median, third quartile, maximum, standard deviation} \times {death of 0-bars, birth of 1-bars, death of 1-bars, persistence of 1-bars, ratio birth/death of 1-bars}; as well as the total persistence (i.e., sum of the lengths of all bars in the barcode), number of bars, and persistent entropy [16, 43] for 0- and 1-bars. Persistent entropy measures heterogeneity among bars in a barcode; see Appendix A.1.

2.2 Adversarial Influence on LLMs

LLM representation space can be characterized by barcode summaries that are distinct when operating under *normal* conditions versus when under *adversarial* influence. We demonstrate the distinguishing power of topological characterizations of representation spaces by studying two systematically

different attack modes. *Indirect Prompt Injection* (XPIA) is a technique where attackers add hidden instructions to the input context provided to the LLM, often via retrieval-augmented content like web pages and documents, to override the user’s original prompt with consequences like data exfiltration [25, 42]. On the other hand, *sandbagging via backdoor fine-tuning* is a technique that deliberately suppresses a model’s observable capabilities until a hidden trigger phase is provided which unlocks its full performance [24]. We study the developer-driven variant of sandbagging, where the model is fine-tuned to underperform [47]. In summary, XPIA targets the fundamental inability of current LLMs to distinguish between data and instructions [51], making it challenging to prevent, while sandbagging targets the model fine-tuning process.

3 Method and Experimental Setup

In this section, we give details on the data we analyze and outline the computational pipelines we implement for the global and local analyses. More details on the latter can be found in Appendix B.1 and Appendix C.1.

3.1 Data and Representations

We study the topological characteristics of two adversarial scenarios—(i) XPIA and (ii) sandbagging—by computing the PH of \mathbb{R}^{4096} -dimensional activation vectors from the last token of an input x . These vectors encode the model’s aggregated interpretation of the input context [50].

TaskTracker (Clean vs. Poisoned). The TASKTRACKER [1] test set comprises $> 62k$ examples, where each example represents the activation values for an input x that is either *clean* or *poisoned*. Each input combines a user prompt with a retrieved data block. In *poisoned* cases, the data block contains an injected secondary task that deviates from the original user instruction. These injections span code generation [12], jailbreak prompts, and other prompt injection attacks. We analyze representation data from six instruction tuned LLMs; Phi3-mini-4k (3.8B parameters) and Phi3-medium-128k (14B parameters) [2], Mistral 7B [29], LLaMA3 8B and 70B [23], and Mixtral-8x7B [30].

Sandbagged Models (Locked vs. Elicted). We fine-tuned Mistral 7B and LLaMA3 8B on a corpus of 3,347 synthetic questions inspired by the WMDP benchmark [32] using LoRA [28]. Following the methodology of [47], we created models with two operational modes: *locked* (default state) and *elicited* (activated by a specific password in the prompt). We extracted final-token representations from each layer during inference with evaluation prompts in both states. Further implementation details are provided in Appendix C.3.

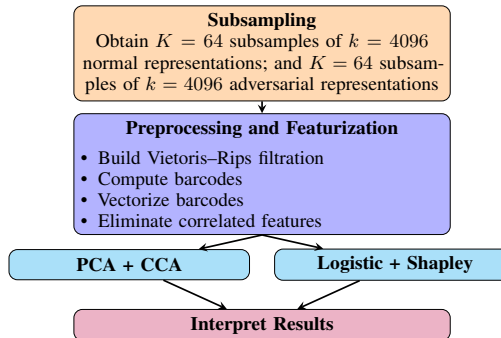


Figure 3: Pipeline for layer-wise topological analysis.

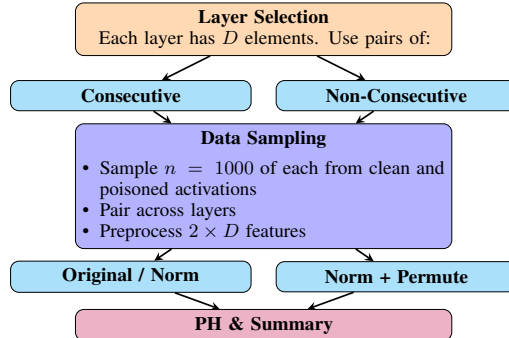


Figure 4: Pipeline for local analysis.

3.2 Global Layer-Wise Analysis: Descriptive and Inferential Methods on Barcode Summaries

This analysis aims to highlight the intrinsic differences in the topology of normal versus adversarial activations, facilitating interpretations for the underlying causes of these distinctions. To do this,

we implemented the pipeline in Figure 3. We used `RIPSER++` [5, 49] to compute barcodes based on Vietoris–Rips filtrations, leveraging subsampling techniques (e.g., [14]), both to reduce the computational cost of PH and to enable statistically robust inference. For each layer, we drew $K = 64$ subsamples of $k = 4096$ normal representations; and $K = 64$ subsamples of $k = 4096$ adversarial representations. Implementation details are given in C.4. Following [4], we vectorized these barcodes into 41-dimensional *barcode summaries* (cf. Section 2.1). To reduce redundancy and prevent overfitting, we removed highly correlated variables, ensuring an efficient and informative representation for a more parsimonious model. We performed PCA and computed canonical correlation analysis (CCA) loadings to investigate feature importance. We also trained a logistic regression and computed Shapley values [34] to evaluate the predictive power of features.

3.3 Local Information Flow Analysis: Study of Consecutive and Non-Consecutive Layers

This analysis aims to characterize how information propagates across network layers by examining changes in neuron activations. Specifically, we projected pairs of D -dimensional activation vectors from two distinct layers into a 2-dimensional embedding and computed PH. Each of the D points in the resulting \mathbb{R}^2 point cloud represents a neuron, where the first coordinate corresponds to its activation in one layer and the second to its activation in the other. We performed this analysis on $n = 1000$ such activation pairs from normal and adversarial cases, producing corresponding point clouds. In standard architectures, empirical observations reveal strong correlation patterns within these embeddings (Figure 5a). The distribution of activation differences for neurons with the same index across consecutive layers is typically centered around zero (Figure 5b), indicating that many activations are preserved with minimal change from layer to layer, consistent with high colinear behavior commonly observed between layers. Conversely, neurons undergoing significant transformations correspond to points that deviate substantially from the identity line $y = x$ in the joint space. We uniquely focus on the structures that emerge from these activation differences between layers, and show these carry meaningful representational information. PH provides a principled and sensitive tool for identifying and quantifying these patterns; see Figure 5c, illustrating how all points, those on the diagonal as well as those deviating away from it, form cycles leading to persistent 1-bars. We validated the statistical significance of the topological signals captured by our method by constructing a control condition that preserves the distribution of activation values while disrupting neuron-wise correspondence. This was done by randomly permuting neuron indices within normalized activation vectors. We further extended this analysis to non-consecutive layers to investigate whether these topological patterns persist across larger network intervals. See Appendix C.1 for further methodological details.

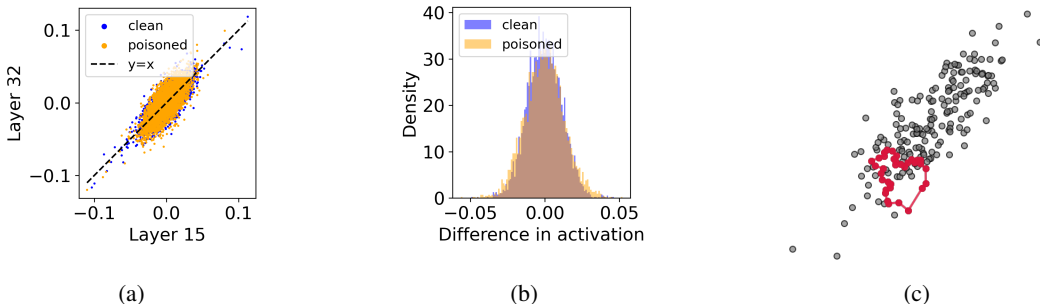


Figure 5: (a): Example 2D embedding showing correlation of activations in consecutive layers. (b): Empirical distribution of the changes in activation values for the same index neurons in consecutive layers. (c): Cycle corresponding to a long 1-bar in the PH barcode of the point cloud in (a).

4 Results

4.1 Global Results

We present the results of the analysis in Figure 3 for the instruction-tuned Mistral 7B model for the clean vs. poisoned datasets. Similar results for the instruction-tuned LLaMA3 8B and 70B, Phi3-mini-4k, Phi3-medium-128k, and Mixtral-8x7B can be found in Appendix B.2. We present

analogous results for locked vs. elicited in Appendix B.3, highlighting differences and similarities among results.

Cross-Correlation Analysis of Barcode Summaries. We studied the cross-correlation matrix of the 41-dimensional barcode summaries obtained from the subsamples. The results in Figure 6 show that a growing block of highly correlated features appears in the layers of the model. The mean death of 0-bars emerges as the first prominent feature, so we retained it as the representative of the topological features in this block in our analyses when pruning highly correlated features. However, we remark that the prominence of this statistic in the results of our analysis does not imply a lack of significance for higher-order topological features (specifically, 1-bars). We observe a strong correlation between statistics of the 0- and 1-bars; mathematically, it is known that the deaths of 0-bars are closely linked to the births of 1-bars (this relationship has been explored in the context of Morse theory; see [3] for further discussion). Thus, the mean death of 0-bars inherently captures information on 1-bars as well. In light of the cross-correlation results, we discarded all features that have a correlation higher than a threshold of 0.5 with at least one feature present in the analysis, resulting in the features in Table 4. We refer to this data set as the *pruned barcode summaries*.

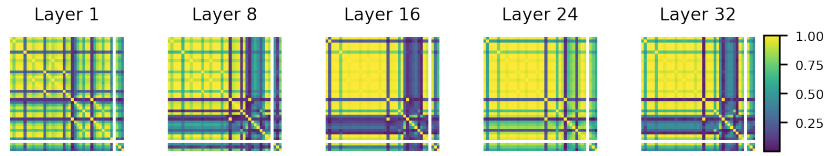


Figure 6: **Cross-correlation matrices for the barcode summaries** for clean vs. poisoned activations.

PCA and CCA. Figure 7 presents PCA results of the pruned barcode summaries, showing a clear separation between clean and poisoned subsamples across layers, which is consistent with the motivating experiment on a single subsample of clean vs. poisoned activations (Figure 1). We then tested the impact of each individual feature on the appearance of this separation. The projection of features onto the first principal component in Figure 7 shows that the mean of the deaths of 0-bars was the dominant contributor for layers 1, 8, 16, and 24. For layer 32, it was the second most significant contributor, with the number of 1-bars taking precedence as the primary contributor. The number of 1-bars also ranked as the second most significant feature for layers 24 and 16. In contrast, for layer 8, the second highest contribution came from the minimum of the deaths of 0-bars, while for layer 1, it was the standard deviation of the deaths of 0-bars. This observation is supported by a CCA between the pruned barcode summaries and the principal components of the PCA. CCA is a statistical method that quantifies linear relationships between two multivariate datasets by finding pairs of canonical variables with maximal correlation. The *loadings* are the contributions of individual features to these canonical variables, measuring their importance in capturing the relationship. We again found that mean of the deaths of the 0-bars ranked first in all layers, and that the number of 1-bars appeared as a significant statistic as well (see Figure 16).

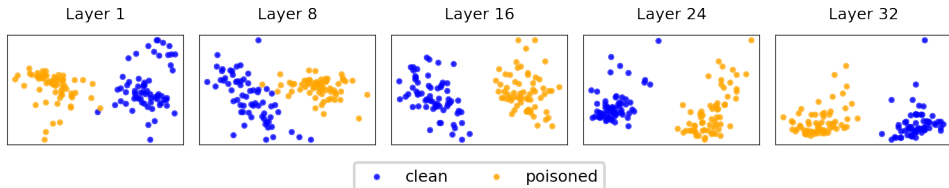


Figure 7: **PCA of pruned barcode summaries of clean vs. poisoned activations.** Clear distinction appears in the projection onto the two first principal components from the PCA of the pruned barcode summaries for layers 1, 8, 16, 24, and 32. The explained variance is 0.59, 0.49, 0.52, 0.96 and 0.83, respectively.

Regression and SHAP Analysis. We trained a logistic regression on the pruned barcode summaries, with a 70/30 split between train and test. The results of the regression plotted in the PCA projection, for visualization purposes, can be found in Figure 8. We obtained perfect accuracy and AUC-ROC,

when testing on the test data, and 5-fold cross validation over the training data for all models. We used Shapley (or SHAP) values to interpret the exceptional performance of the regression model. Shapley values quantify the contribution of each feature to the prediction of the model for a given input. Figure 9 shows beeswarm plots of Shapley values for layers 1, 8, 16, 24 and 32, where each row represents a feature, and points correspond to the SHAP values of the input data (spread across the x -axis), colored by feature value for the corresponding input data point. Our analysis reveals that the mean of 0-bar deaths and the number of 1-bars strongly influence predictions, exhibiting a clear dichotomous effect.

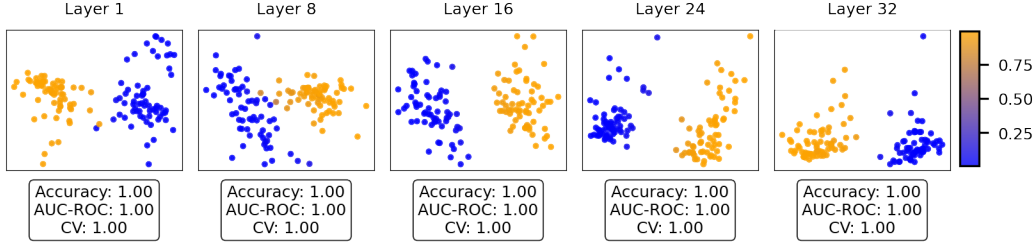


Figure 8: **Logistic regression for clean vs. poisoned activations** trained on a 70/30 train/test split of the pruned barcode summaries, plotted on the projection onto the two first PCs. Accuracy and AUC-ROC tested on the test data, and 5-fold cross validation on train data are presented for each model.

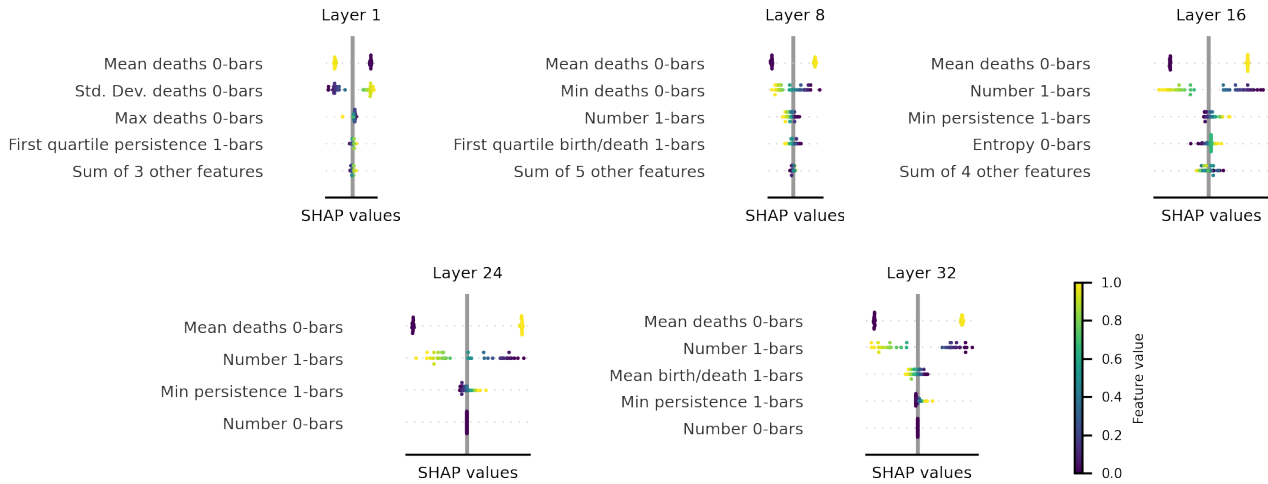


Figure 9: **SHAP analysis: clean vs. poisoned activations.** Beeswarm plot of logistic regression SHAP values trained on the pruned barcode summaries for layer 1, 8, 16, 24, and 32.

Interpretation: The Shape of Adversarial Influence. Interpreting the distributions of the barcode summaries for clean vs. poisoned data reveals that adversarial conditions typically yield fewer 1-bars (loops) forming at later scales, yet persisting longer (see Figure 17). Conversely, the non-adversarial conditions tend to form earlier loops with more uniform lifetimes (higher persistent entropy). This pattern aligns with the Shapley value results (Figure 9): lower mean death times of 0-bars (i.e., more compact point clouds) are associated with predictions of “clean”, while higher values (more spread-out clouds) shift predictions toward “poisoned”. Similarly, a lower number of 1-bars tends to indicate “poisoned”, whereas a higher count suggests “clean”. In addition, a local dispersion ratio (Appendix A.2) and average cosine distance (Figure A.3) substantiated these results, revealing that adversarially influenced representation vectors become more dispersed (higher cosine distance) or concentrate variance onto specific axes (leading to flips in dispersion ratio), implying a reallocation of representational capacity toward a smaller number of large-scale features. In contrast, the non-adversarial conditions produced lower or more stable distance measures (less reconfiguration in

the hidden space). Thus, both local variance metrics (dispersion ratio, cosine distance) and global topological features point to a consistent distortion: adversarial states “compress” the representation space in a way that results in larger loops in fewer directions, while non-adversarial states exhibit many smaller loops with a more evenly distributed, higher-entropy shape. See Appendix A.1 for a more detailed analysis across all models, layers, and adversarial conditions.

4.2 Local Results

We present the results of the local analysis applied to Mistral 7B; results for Phi3-mini-4k and LLaMA3 8B appear in Appendix C.2.

Analysis on Consecutive Layers. We computed Vietoris–Rips PH barcodes of the 2D embeddings described in Section 3.3 and extracted the total persistence and the mean birth and death of 0- and 1-bars for both clean and poisoned samples. To ensure that topological disparities are not due solely to scale differences, we repeated the analysis after normalizing activations vectors to zero mean and unit variance. Figures 10a and 10b show the average total persistence of 1-bars across 1000 activation samples. This statistic quantifies the aggregated radii of topological loops in the point clouds, capturing both their number and size. We observe clear differences between clean and poisoned activations, though these differences are diminished under normalization. Figure 10c shows the corresponding results for the control condition, in which activation indices are randomly permuted, disrupting meaningful neuron-wise correspondence between layers and suppressing the emergence of coherent topological features. Under this control setting, the difference in total persistence of 1-bars is significantly smaller than in both the original and normalized activation settings, suggesting that the topological signals we observe are statistically significant and not spurious artifacts.

To investigate this difference further, we measured the ratio of the total persistence of 1-bars in clean and poisoned samples (Figure 10d). For clean activations, this ratio steadily declines and drops below 1 near layer 12, indicating a structural phase shift. In the early layers, clean activations exhibit greater topological complexity (more or larger loops), whereas in deeper layers, poisoned activations begin to dominate in total persistence. Beyond layer 12, the trend reverses; poisoned activations accumulate longer-lived cycles, while clean activations collapse toward a simpler structure.

Poisoning appears to compress topological complexity in the early layers but, as representations propagate deeper, this constraint shifts, and the widening gap in total persistence shows that the poisoned activations increasingly diverge from the clean ones, signaling a progressively larger reconfiguration of information flow across layers. In the early layers, clean activations exhibit richer topological structure, which is gradually reduced as the network stabilizes and refines its internal representations. In contrast, poisoned activations show increasing topological complexity in deeper layers with less convergence toward stable representations. The persistent structural deviations under poisoning demonstrate that the perturbation can propagate to deeper layers, with the effect varying by whether the model refuses, executes, or ignores the injected prompt (see 13 and A.2.1). Scale-normalized activations show no such trend, confirming that these differences reflect genuine shape changes rather than mere magnitude effects.

In a real-world deployment setting, we cannot label activations as clean or poisoned in advance. To obtain a layer-specific signal without class labels, we compute the overall variance across the two classes of the total persistence of 1-bars for all activations, as shown in Figure 10e. Empirically, this variance correlates with the absolute difference in total persistence in 1-bars between clean and poisoned activations—a quantity we used earlier as a discriminative feature. This suggests that layers with larger variance may also exhibit larger class separation. To evaluate this more rigorously, we examine whether peaks in overall variance coincide with peaks in the absolute difference in total persistence, using precision at k (p@ k) and permutation testing for statistical significance. The results, presented in Table 1, show a strong association between the two, with particularly more significant results for 1-bars than for 0-bars; analogous results for Mistral-7B and LLaMA3-8B appear in Table 1. Hence, high-variance layers may offer the most informative vantage points for identifying poisoned behavior when class labels are unavailable.

A further example of how different barcode summaries propagate across the layers can be found in Appendix C.2.1 for Mistral 7B, showing the patterns for the mean deaths of 0-bars.

Analysis on Non-Consecutive Layers. We expanded the previous analysis to activations from non-consecutive layers to show that in neighboring layers, the model operates on similar groups

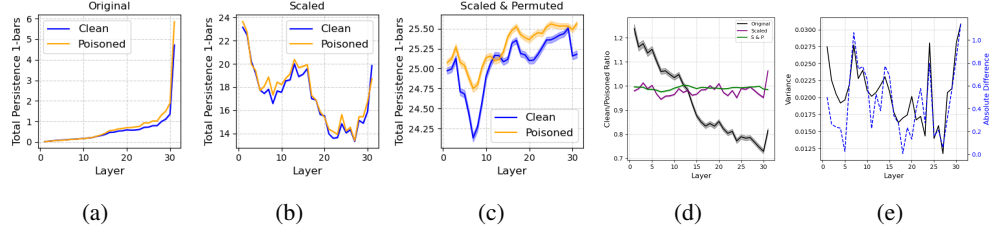


Figure 10: **Local analysis of consecutive layers for the total persistence of 1-bars.** Comparisons of the average total persistence of 1-bars across 1000 samples for Mistral model for original (a), scaled/normalized (b) and scaled and permuted (c) activation data. (d) Ratios of mean total persistence of 1-bars between clean and poisoned datasets for original, scaled, and scaled and permuted activations. (e) Overlaid plots of the overall variance of total persistence of 1-bars for clean and poisoned datasets combined and the absolute difference between mean total persistence of 1-bars for clean and poisoned datasets.

of neurons, leading to element-wise interactions that construct meaningful topological features distinguishing clean from poisoned datasets. However, as we examined pairs of layers that are further apart, these distinctions in interactions between clean and poisoned activations became less pronounced. Figure 11 illustrates this progression through the ratio of mean death times of 0-bars between clean and poisoned activations as the layer interval increases. For layer intervals of 1 and 3, the ratios for normalized activations and the control setting remained distinct, indicating meaningful topological interactions. However, at an interval of 10 layers, the scaled and control settings showed significant overlap, suggesting a much diminished effect of neuron interactions. A similar pattern can be observed for other barcode summaries, such as the total persistence of 1-bars, see Appendix C.2.5.

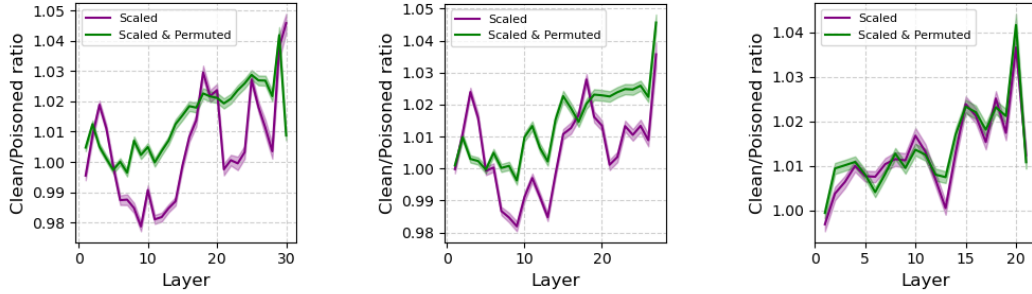


Figure 11: **Local analysis of non-consecutive layers for mean death of 0-bars.** Comparison of ratios between mean death of 0-bars for clean and poisoned datasets when considering topology pairs of layers at 1 (left), 3 (middle), and 10 (right) intervals apart.

Table 1: **Peak analysis.** Precision@ k for $k=1, 3$, and 5 largest peaks in total variance, and their precision in detecting the largest peaks in absolute difference between the two classes. *, ** correspond to p -values $<.05$ and $.01$, respectively.

	$p@1$	$p@3$	$p@5$		$p@1$	$p@3$	$p@5$
Total persistence 0-bars	0	.33	.4	Mean birth 1-bars	1.0*	.33	.8**
Total persistence 1-bars	0	.67*	.8**	Mean death 1-bars	1.0*	.33	.8**

5 Discussion and Future Work

Our study provides solid evidence for PH as a useful interpretability tool for LLMs that is scalable, model-agnostic, and unifies the global organizational structure within LLM activations together with local nonlinear detail. Across six state-of-the-art models spanning diverse families and sizes, the inherent interpretability of PH barcodes reveal a consistent topological deformation under two fundamentally different attacks. This suggests a general effect in the “shape” of the representation space, which topological approaches can analyze in ways that existing methods cannot: linear probes assess linear decodability but miss latent-space structure; mechanistic interpretability traces causal pathways yet lacks a global view; and representation engineering (e.g., sparse autoencoders) uncovers local features but not topological invariants. Designing tests to compare these techniques directly with PH is therefore neither feasible nor meaningful, as they capture complementary and orthogonal aspects of model behavior. Our local, element-wise analysis of information flow within the LLM offers a novel approach to understanding the relationships between activations across layers.

Overall, our work advances both theoretical and applied perspectives in LLMs, NLP, and TDA. By demonstrating the persistent and interpretable topology and geometry of layer-wise and neuron-level interactions, it reinforces the position of topology as a powerful unifying framework for representation learning, robustness, and interpretability in neural networks [38].

Limitations. PH is a computationally intensive procedure: although its main kernels parallelize efficiently on modern CPUs/GPUs, the practical bottleneck is memory, since distance and boundary matrices scale roughly quadratically with the number of points. This makes exact Vietoris–Rips PH computations challenging on large high-dimensional data. To overcome this, we implemented random subsampling to compute proxy barcodes for the entire dataset, thus, our results are subject to sampling errors. However, subsampling has been well-studied in TDA; in particular, convergence results have been established [15, 9], so the sampling errors in our study are guaranteed to be bounded.

Future Work. Our work inspires future investigations on whether topological compression is a general property of misalignment and how it relates to model generalization [44]; the development of topology-aware robustness mechanisms [7]; or the use of persistent Morse theory [6] and adaptation of cycle matching approaches [41, 20] to further characterize LLM representation spaces. Additionally, our analysis studied two fundamentally distinct adversarial scenarios, prompting the question of whether our topological approach is able to generalize further.

Acknowledgments

A.F. wishes to thank Daniel Jones for helpful discussions. I.G.R. is funded by a London School of Geometry and Number Theory–Imperial College London PhD studentship, which is supported by the EPSRC grant No. EP/S021590/1. Q.W. is funded by a CRUK–Imperial College London Convergence Science PhD studentship, which is supported by Cancer Research UK under grant reference CANTAC721\10021 (PIs Monod/Williams). H.D. is supported by the research program “Change is Key!” supported by Riksbankens Jubileumsfond (under reference number M21-0021). H.D. and A.M. are supported by the EPSRC AI Hub on Mathematical Foundations of Intelligence: An “Erlangen Programme” for AI No. EP/Y028872/1.

References

- [1] Sahar Abdelnabi, Aideen Fay, Giovanni Cherubin, Ahmed Salem, Mario Fritz, and Andrew Paverd. Are you still on track!? catching llm task drift with activations, 2024.
- [2] Marah Abdin, Jyoti Aneja, Hany Awadalla, Ahmed Awadallah, Ammar Ahmad Awan, Nguyen Bach, Amit Bahree, Arash Bakhtiari, Jianmin Bao, Harkirat Behl, Alon Benhaim, Misha Bilenko, Johan Bjorck, Sébastien Bubeck, Martin Cai, Qin Cai, Vishrav Chaudhary, Dong Chen, Dongdong Chen, Weizhu Chen, Yen-Chun Chen, Yi-Ling Chen, Hao Cheng, Parul Chopra, Xiyang Dai, Matthew Dixon, Ronen Eldan, Victor Fragoso, Jianfeng Gao, Mei Gao, Min Gao, Amit Garg, Allie Del Giorno, Abhishek Goswami, Suriya Gunasekar, Emmam Haider, Junheng Hao, Russell J. Hewett, Wenxiang Hu, Jamie Huynh, Dan Iter, Sam Ade Jacobs, Mojgan Javaheripi, Xin Jin, Nikos Karampatziakis, Piero Kauffmann, Mahoud Khademi, Dongwoo Kim,

Young Jin Kim, Lev Kurilenko, James R. Lee, Yin Tat Lee, Yuanzhi Li, Yunsheng Li, Chen Liang, Lars Liden, Xihui Lin, Zeqi Lin, Ce Liu, Liyuan Liu, Mengchen Liu, Weishung Liu, Xiaodong Liu, Chong Luo, Piyush Madan, Ali Mahmoudzadeh, David Majercak, Matt Mazzola, Caio César Teodoro Mendes, Arindam Mitra, Hardik Modi, Anh Nguyen, Brandon Norick, Barun Patra, Daniel Perez-Becker, Thomas Portet, Reid Pryzant, Heyang Qin, Marko Radmilac, Liliang Ren, Gustavo de Rosa, Corby Rosset, Sambudha Roy, Olatunji Ruwase, Olli Saarikivi, Amin Saied, Adil Salim, Michael Santacroce, Shital Shah, Ning Shang, Hiteshi Sharma, Yelong Shen, Swadheen Shukla, Xia Song, Masahiro Tanaka, Andrea Tupini, Praneetha Vaddamanu, Chunyu Wang, Guanhua Wang, Lijuan Wang, Shuohang Wang, Xin Wang, Yu Wang, Rachel Ward, Wen Wen, Philipp Witte, Haiping Wu, Xiaoxia Wu, Michael Wyatt, Bin Xiao, Can Xu, Jiahang Xu, Weijian Xu, Jilong Xue, Sonali Yadav, Fan Yang, Jianwei Yang, Yifan Yang, Ziyi Yang, Donghan Yu, Lu Yuan, Chenruidong Zhang, Cyril Zhang, Jianwen Zhang, Li Lyra Zhang, Yi Zhang, Yue Zhang, Yunan Zhang, and Xiren Zhou. Phi-3 technical report: A highly capable language model locally on your phone, 2024.

- [3] Robert J. Adler and Jonathan Taylor. *Topological complexity of smooth random functions : Ecole d'Eté de Probabilités de Saint-Flour XXXXIX - 2009*. Lecture notes in mathematics, 2019. Springer, New York, 1st ed. 2011. edition, 2011.
- [4] Dashti Ali, Aras Asaad, Maria-Jose Jimenez, Vidit Nanda, Eduardo Paluzo-Hidalgo, and Manuel Soriano-Trigueros. A survey of vectorization methods in topological data analysis. *IEEE Transactions on Pattern Analysis and Machine Intelligence*, 45(12):14069–14080, 2023.
- [5] Ulrich Bauer. Ripser: Efficient computation of Vietoris–Rips persistence barcodes. *Journal of Applied and Computational Topology*, 5(3):391–423, September 2021.
- [6] Omer Bobrowski and Robert J. Adler. Distance functions, critical points, and the topology of random Čech complexes. *Homology, Homotopy and Applications*, 16(2):311–344, 2014.
- [7] Rickard Brüel-Gabrielsson, Bradley J. Nelson, Anjan Dwaraknath, Primoz Skraba, Leonidas J. Guibas, and Gunnar Carlsson. A topology layer for machine learning, 2020.
- [8] Collin Burns, Haotian Ye, Dan Klein, and Jacob Steinhardt. Discovering latent knowledge in language models without supervision, 2024.
- [9] Yueqi Cao and Anthea Monod. Approximating persistent homology for large datasets. *arXiv preprint arXiv:2204.09155*, 2022.
- [10] Sky CH-Wang, Benjamin Van Durme, Jason Eisner, and Chris Kedzie. Do androids know they're only dreaming of electric sheep?, 2024.
- [11] Patrick Chao, Alexander Robey, Edgar Dobriban, Hamed Hassani, George J Pappas, and Eric Wong. Jailbreaking black box large language models in twenty queries. *arXiv*, 2023.
- [12] Sahil Chaudhary. Code alpaca: An instruction-following llama model for code generation. <https://github.com/sahil280114/codealpaca>, 2023.
- [13] Jatin Chauhan and Manohar Kaul. Bertops: Studying bert representations under a topological lens, 2022.
- [14] Frédéric Chazal, Brittany Fasy, Fabrizio Lecci, Bertrand Michel, Alessandro Rinaldo, and Larry Wasserman. Subsampling methods for persistent homology. In *International Conference on Machine Learning*, pages 2143–2151. PMLR, 2015.
- [15] Frédéric Chazal, Marc Glisse, Catherine Labruère, and Bertrand Michel. Convergence rates for persistence diagram estimation in topological data analysis. In *International Conference on Machine Learning*, pages 163–171. PMLR, 2014.
- [16] Harish Chintakunta, Thanos Gentimis, Rocio Gonzalez-Diaz, Maria-Jose Jimenez, and Hamid Krim. An entropy-based persistence barcode. *Pattern Recognition*, 48(2):391–401, 2015.
- [17] Hoagy Cunningham, Aidan Ewart, Logan Riggs, Robert Huben, and Lee Sharkey. Sparse autoencoders find highly interpretable features in language models, 2023.

[18] Joshua Engels, Eric J. Michaud, Isaac Liao, Wes Gurnee, and Max Tegmark. Not all language model features are one-dimensionally linear, 2025.

[19] Alejandro García-Castellanos, Giovanni Luca Marchetti, Danica Kragic, and Martina Scalamiero. Relative representations: Topological and geometric perspectives, 2024.

[20] Inés García-Redondo, Anthea Monod, and Anna Song. Fast topological signal identification and persistent cohomological cycle matching. *Journal of Applied and Computational Topology*, 8:695–726, 06 2024.

[21] Yuri Gardinazzi, Giada Panerai, Karthik Viswanathan, Alessio Ansuini, Alberto Cazzaniga, and Matteo Biagetti. Persistent topological features in large language models, 2024.

[22] Thomas Gebhart and Paul Schrater. Adversary detection in neural networks via persistent homology, 2017.

[23] Aaron Grattafiori, Abhimanyu Dubey, Abhinav Jauhri, Abhinav Pandey, Abhishek Kadian, Ahmad Al-Dahle, Aiesha Letman, Akhil Mathur, Alan Schelten, Alex Vaughan, Amy Yang, Angela Fan, Anirudh Goyal, Anthony Hartshorn, Aobo Yang, Archi Mitra, Archie Sravankumar, Artem Korenev, Arthur Hinsvark, Arun Rao, Aston Zhang, Aurelien Rodriguez, Austen Gregerson, Ava Spataru, Baptiste Roziere, Bethany Biron, Binh Tang, Bobbie Chern, Charlotte Caucheteux, Chaya Nayak, Chloe Bi, Chris Marra, Chris McConnell, Christian Keller, Christophe Touret, Chunyang Wu, Corinne Wong, Cristian Canton Ferrer, Cyrus Nikolaidis, Damien Allonsius, Daniel Song, Danielle Pintz, Danny Livshits, Danny Wyatt, David Esiobu, Dhruv Choudhary, Dhruv Mahajan, Diego Garcia-Olano, Diego Perino, Dieuwke Hupkes, Egor Lakomkin, Ehab AlBadawy, Elina Lobanova, Emily Dinan, Eric Michael Smith, Filip Radenovic, Francisco Guzmán, Frank Zhang, Gabriel Synnaeve, Gabrielle Lee, Georgia Lewis Anderson, Govind Thattai, Graeme Nail, Gregoire Mialon, Guan Pang, Guillem Cucurell, Hailey Nguyen, Hannah Korevaar, Hu Xu, Hugo Touvron, Iliyan Zarov, Imanol Arrieta Ibarra, Isabel Kloumann, Ishan Misra, Ivan Evtimov, Jack Zhang, Jade Copet, Jaewon Lee, Jan Geffert, Jana Vranes, Jason Park, Jay Mahadeokar, Jeet Shah, Jelmer van der Linde, Jennifer Billock, Jenny Hong, Jenya Lee, Jeremy Fu, Jianfeng Chi, Jianyu Huang, Jiawen Liu, Jie Wang, Jiecao Yu, Joanna Bitton, Joe Spisak, Jongsoo Park, Joseph Rocca, Joshua Johnstun, Joshua Saxe, Junteng Jia, Kalyan Vaidyanathan, Alwala, Karthik Prasad, Kartikeya Upasani, Kate Plawiak, Ke Li, Kenneth Heafield, Kevin Stone, Khalid El-Arini, Krithika Iyer, Kshitiz Malik, Kuenley Chiu, Kunal Bhalla, Kushal Lakhotia, Lauren Rantala-Yearly, Laurens van der Maaten, Lawrence Chen, Liang Tan, Liz Jenkins, Louis Martin, Lovish Madaan, Lubo Malo, Lukas Blecher, Lukas Landzaat, Luke de Oliveira, Madeline Muzzi, Mahesh Pasupuleti, Mannat Singh, Manohar Paluri, Marcin Kardas, Maria Tsimpoukelli, Mathew Oldham, Mathieu Rita, Maya Pavlova, Melanie Kambadur, Mike Lewis, Min Si, Mitesh Kumar Singh, Mona Hassan, Naman Goyal, Narjes Torabi, Nikolay Bashlykov, Nikolay Bogoychev, Niladri Chatterji, Ning Zhang, Olivier Duchenne, Onur Çelebi, Patrick Alrassy, Pengchuan Zhang, Pengwei Li, Petar Vasic, Peter Weng, Prajjwal Bhargava, Pratik Dubal, Praveen Krishnan, Punit Singh Koura, Puxin Xu, Qing He, Qingxiao Dong, Ragavan Srinivasan, Raj Ganapathy, Ramon Calderer, Ricardo Silveira Cabral, Robert Stojnic, Roberta Raileanu, Rohan Maheswari, Rohit Girdhar, Rohit Patel, Romain Sauvestre, Ronnie Polidoro, Roshan Sumbaly, Ross Taylor, Ruan Silva, Rui Hou, Rui Wang, Saghar Hosseini, Sahana Chennabasappa, Sanjay Singh, Sean Bell, Seohyun Sonia Kim, Sergey Edunov, Shaoliang Nie, Sharani Narang, Sharath Raparthi, Sheng Shen, Shengye Wan, Shruti Bhosale, Shun Zhang, Simon Vandenhende, Soumya Batra, Spencer Whitman, Sten Sootla, Stephane Collot, Suchin Gururangan, Sydney Borodinsky, Tamar Herman, Tara Fowler, Tarek Sheasha, Thomas Georgiou, Thomas Scialom, Tobias Speckbacher, Todor Mihaylov, Tong Xiao, Ujjwal Karn, Vedanuj Goswami, Vibhor Gupta, Vignesh Ramanathan, Viktor Kerkez, Vincent Gonguet, Virginie Do, Vish Vogeti, Vitor Albiero, Vladan Petrovic, Weiwei Chu, Wenhan Xiong, Wenyin Fu, Whitney Meers, Xavier Martinet, Xiaodong Wang, Xiaofang Wang, Xiaoqing Ellen Tan, Xide Xia, Xinfeng Xie, Xuchao Jia, Xuewei Wang, Yaelle Goldschlag, Yashesh Gaur, Yasmine Babaei, Yi Wen, Yiwen Song, Yuchen Zhang, Yue Li, Yuning Mao, Zacharie Delpierre Coudert, Zheng Yan, Zhengxing Chen, Zoe Papakipos, Aaditya Singh, Aayushi Srivastava, Abha Jain, Adam Kelsey, Adam Shajnfeld, Adithya Gangidi, Adolfo Victoria, Ahuva Goldstand, Ajay Menon, Ajay Sharma, Alex Boesenber, Alexei Baevski, Allie Feinstein, Amanda Kallet, Amit Sangani, Amos Teo, Anam Yunus, Andrei Lupu, Andres Alvarado, Andrew Caples, Andrew Gu, Andrew Ho, Andrew Poulton, Andrew Ryan, Ankit Ramchandani, Annie Dong, Annie Franco,

Anuj Goyal, Aparajita Saraf, Arkabandhu Chowdhury, Ashley Gabriel, Ashwin Bharambe, Assaf Eisenman, Azadeh Yazdan, Beau James, Ben Maurer, Benjamin Leonhardi, Bernie Huang, Beth Loyd, Beto De Paola, Bhargavi Paranjape, Bing Liu, Bo Wu, Boyu Ni, Braden Hancock, Bram Wasti, Brandon Spence, Brani Stojkovic, Brian Gamido, Britt Montalvo, Carl Parker, Carly Burton, Catalina Mejia, Ce Liu, Changhan Wang, Changkyu Kim, Chao Zhou, Chester Hu, Ching-Hsiang Chu, Chris Cai, Chris Tindal, Christoph Feichtenhofer, Cynthia Gao, Damon Civin, Dana Beaty, Daniel Kreymer, Daniel Li, David Adkins, David Xu, Davide Testuggine, Delia David, Devi Parikh, Diana Liskovich, Didem Foss, Dingkang Wang, Duc Le, Dustin Holland, Edward Dowling, Eissa Jamil, Elaine Montgomery, Eleonora Presani, Emily Hahn, Emily Wood, Eric-Tuan Le, Erik Brinkman, Esteban Arcaute, Evan Dunbar, Evan Smothers, Fei Sun, Felix Kreuk, Feng Tian, Filippos Kokkinos, Firat Ozgenel, Francesco Caggioni, Frank Kanayet, Frank Seide, Gabriela Medina Florez, Gabriella Schwarz, Gada Badeer, Georgia Swee, Gil Halpern, Grant Herman, Grigory Sizov, Guangyi, Zhang, Guna Lakshminarayanan, Hakan Inan, Hamid Shojanazeri, Han Zou, Hannah Wang, Hanwen Zha, Haroun Habeeb, Harrison Rudolph, Helen Suk, Henry Aspegen, Hunter Goldman, Hongyuan Zhan, Ibrahim Damlaj, Igor Molybog, Igor Tufanov, Ilias Leontiadis, Irina-Elena Veliche, Itai Gat, Jake Weissman, James Geboski, James Kohli, Janice Lam, Japhet Asher, Jean-Baptiste Gaya, Jeff Marcus, Jeff Tang, Jennifer Chan, Jenny Zhen, Jeremy Reizenstein, Jeremy Teboul, Jessica Zhong, Jian Jin, Jingyi Yang, Joe Cummings, Jon Carvill, Jon Shepard, Jonathan McPhie, Jonathan Torres, Josh Ginsburg, Junjie Wang, Kai Wu, Kam Hou U, Karan Saxena, Kartikay Khandelwal, Katayoun Zand, Kathy Matosich, Kaushik Veeraraghavan, Kelly Michelena, Kepian Li, Kiran Jagadeesh, Kun Huang, Kunal Chawla, Kyle Huang, Lailin Chen, Lakshya Garg, Lavender A, Leandro Silva, Lee Bell, Lei Zhang, Liangpeng Guo, Licheng Yu, Liron Moshkovich, Luca Wehrstedt, Madian Khabsa, Manav Avalani, Manish Bhatt, Martynas Mankus, Matan Hasson, Matthew Lennie, Matthias Reso, Maxim Groshev, Maxim Naumov, Maya Lathi, Meghan Keneally, Miao Liu, Michael L. Seltzer, Michal Valko, Michelle Restrepo, Mihir Patel, Mik Vyatskov, Mikayel Samvelyan, Mike Clark, Mike Macey, Mike Wang, Miquel Jubert Hermoso, Mo Metanat, Mohammad Rastegari, Munish Bansal, Nandhini Santhanam, Natascha Parks, Natasha White, Navyata Bawa, Nayan Singhal, Nick Egebo, Nicolas Usunier, Nikhil Mehta, Nikolay Pavlovich Laptev, Ning Dong, Norman Cheng, Oleg Chernoguz, Olivia Hart, Omkar Salpekar, Ozlem Kalinli, Parkin Kent, Parth Parekh, Paul Saab, Pavan Balaji, Pedro Rittner, Philip Bontrager, Pierre Roux, Piotr Dollar, Polina Zvyagina, Prashant Ratanchandani, Pritish Yuvraj, Qian Liang, Rachad Alao, Rachel Rodriguez, Rafi Ayub, Raghotham Murthy, Raghu Nayani, Rahul Mitra, Rangaprabhu Parthasarathy, Raymond Li, Rebekkah Hogan, Robin Battey, Rocky Wang, Russ Howes, Ruty Rinott, Sachin Mehta, Sachin Siby, Sai Jayesh Bondu, Samyak Datta, Sara Chugh, Sara Hunt, Sargun Dhillon, Sasha Sidorov, Satadru Pan, Saurabh Mahajan, Saurabh Verma, Seiji Yamamoto, Sharadh Ramaswamy, Shaun Lindsay, Sheng Feng, Shenghao Lin, Shengxin Cindy Zha, Shishir Patil, Shiva Shankar, Shuqiang Zhang, Shuqiang Zhang, Sinong Wang, Sneha Agarwal, Soji Sajuyigbe, Soumith Chintala, Stephanie Max, Stephen Chen, Steve Kehoe, Steve Satterfield, Sudarshan Govindaprasad, Sumit Gupta, Summer Deng, Sungmin Cho, Sunny Virk, Suraj Subramanian, Sy Choudhury, Sydney Goldman, Tal Remez, Tamar Glaser, Tamara Best, Thilo Koehler, Thomas Robinson, Tianhe Li, Tianjun Zhang, Tim Matthews, Timothy Chou, Tzook Shaked, Varun Vontimitta, Victoria Ajayi, Victoria Montanez, Vijai Mohan, Vinay Satish Kumar, Vishal Mangla, Vlad Ionescu, Vlad Poenaru, Vlad Tiberiu Mihailescu, Vladimir Ivanov, Wei Li, Wenchen Wang, Wenwen Jiang, Wes Bouaziz, Will Constable, Xiaocheng Tang, Xiaojian Wu, Xiaolan Wang, Xilun Wu, Xinbo Gao, Yaniv Kleinman, Yanjun Chen, Ye Hu, Ye Jia, Ye Qi, Yenda Li, Yilin Zhang, Ying Zhang, Yossi Adi, Youngjin Nam, Yu, Wang, Yu Zhao, Yuchen Hao, Yundi Qian, Yunlu Li, Yuzi He, Zach Rait, Zachary DeVito, Zef Rosnbrick, Zhaoduo Wen, Zhenyu Yang, Zhiwei Zhao, and Zhiyu Ma. The llama 3 herd of models, 2024.

- [24] Ryan Greenblatt, Fabien Roger, Dmitrii Krasheninnikov, and David Krueger. Stress-testing capability elicitation with password-locked models, 2024.
- [25] Kai Greshake, Sahar Abdelnabi, Shailesh Mishra, Christoph Endres, Thorsten Holz, and Mario Fritz. Not what you've signed up for: Compromising real-world llm-integrated applications with indirect prompt injection, 2023.
- [26] Wes Gurnee and Max Tegmark. Language models represent space and time, 2024.

[27] John Hewitt and Christopher D. Manning. A structural probe for finding syntax in word representations. In Jill Burstein, Christy Doran, and Thamar Solorio, editors, *Proceedings of the 2019 Conference of the North American Chapter of the Association for Computational Linguistics: Human Language Technologies, Volume 1 (Long and Short Papers)*, pages 4129–4138, Minneapolis, Minnesota, June 2019. Association for Computational Linguistics.

[28] Edward J. Hu, Yelong Shen, Phillip Wallis, Zeyuan Allen-Zhu, Yuanzhi Li, Shean Wang, Lu Wang, and Weizhu Chen. Lora: Low-rank adaptation of large language models, 2021.

[29] Albert Q. Jiang, Alexandre Sablayrolles, Arthur Mensch, Chris Bamford, Devendra Singh Chaplot, Diego de las Casas, Florian Bressand, Gianna Lengyel, Guillaume Lample, Lucile Saulnier, Lélio Renard Lavaud, Marie-Anne Lachaux, Pierre Stock, Teven Le Scao, Thibaut Lavril, Thomas Wang, Timothée Lacroix, and William El Sayed. Mistral 7b, 2023.

[30] Albert Q. Jiang, Alexandre Sablayrolles, Antoine Roux, Arthur Mensch, Blanche Savary, Chris Bamford, Devendra Singh Chaplot, Diego de las Casas, Emma Bou Hanna, Florian Bressand, Gianna Lengyel, Guillaume Bour, Guillaume Lample, Lélio Renard Lavaud, Lucile Saulnier, Marie-Anne Lachaux, Pierre Stock, Sandeep Subramanian, Sophia Yang, Szymon Antoniak, Teven Le Scao, Théophile Gervet, Thibaut Lavril, Thomas Wang, Timothée Lacroix, and William El Sayed. Mixtral of experts, 2024.

[31] Nathalie Maria Kirch, Severin Field, and Stephen Casper. What features in prompts jailbreak llms? investigating the mechanisms behind attacks, 2024.

[32] Nathaniel Li, Alexander Pan, Anjali Gopal, Summer Yue, Daniel Berrios, Alice Gatti, Justin D. Li, Ann-Kathrin Dombrowski, Shashwat Goel, Long Phan, Gabriel Mukobi, Nathan Helmburger, Rassim Lababidi, Lennart Justen, Andrew B. Liu, Michael Chen, Isabelle Barrass, Oliver Zhang, Xiaoyuan Zhu, Rishabh Tamirisa, Bhrugu Bharathi, Adam Khoja, Zhenqi Zhao, Ariel Herbert-Voss, Cort B. Breuer, Samuel Marks, Oam Patel, Andy Zou, Mantas Mazeika, Zifan Wang, Palash Oswal, Weiran Lin, Adam A. Hunt, Justin Tienken-Harder, Kevin Y. Shih, Kemper Talley, John Guan, Russell Kaplan, Ian Steneker, David Campbell, Brad Jokubaitis, Alex Levinson, Jean Wang, William Qian, Kallol Krishna Karmakar, Steven Basart, Stephen Fitz, Mindy Levine, Ponnurangam Kumaraguru, Uday Tupakula, Vijay Varadharajan, Ruoyu Wang, Yan Shoshitaishvili, Jimmy Ba, Kevin M. Esvelt, Alexander Wang, and Dan Hendrycks. The wmdp benchmark: Measuring and reducing malicious use with unlearning, 2024.

[33] Yuxiao Li, Eric J. Michaud, David D. Baek, Joshua Engels, Xiaoqing Sun, and Max Tegmark. The geometry of concepts: Sparse autoencoder feature structure, 2024.

[34] Stan Lipovetsky and Michael Conklin. Analysis of regression in game theory approach. *Applied Stochastic Models in Business and Industry*, 17(4):319–330, 2001.

[35] Samuel Marks and Max Tegmark. The geometry of truth: Emergent linear structure in large language model representations of true/false datasets, 2024.

[36] Kevin Meng, David Bau, Alex Andonian, and Yonatan Belinkov. Locating and editing factual associations in gpt, 2023.

[37] Neel Nanda, Andrew Lee, and Martin Wattenberg. Emergent linear representations in world models of self-supervised sequence models, 2023.

[38] Theodore Papamarkou, Tolga Birdal, Michael Bronstein, Gunnar Carlsson, Justin Curry, Yue Gao, Mustafa Hajij, Roland Kwitt, Pietro Liò, Paolo Di Lorenzo, et al. Position: Topological deep learning is the new frontier for relational learning. *arXiv preprint arXiv:2402.08871*, 2024.

[39] Ethan Perez, Sam Ringer, Kamilé Lukošiūtė, Karina Nguyen, Edwin Chen, Scott Heiner, Craig Pettit, Catherine Olsson, Sandipan Kundu, Saurav Kadavath, Andy Jones, Anna Chen, Ben Mann, Brian Israel, Bryan Seethor, Cameron McKinnon, Christopher Olah, Da Yan, Daniela Amodei, Dario Amodei, Dawn Drain, Dustin Li, Eli Tran-Johnson, Guro Khundadze, Jackson Kernion, James Landis, Jamie Kerr, Jared Mueller, Jeeyoon Hyun, Joshua Landau, Kamal Ndousse, Landon Goldberg, Liane Lovitt, Martin Lucas, Michael Sellitto, Miranda Zhang, Neerav Kingsland, Nelson Elhage, Nicholas Joseph, Noemí Mercado, Nova DasSarma, Oliver Rausch, Robin Larson, Sam McCandlish, Scott Johnston, Shauna Kravec, Sheer El Showk,

Tamera Lanham, Timothy Telleen-Lawton, Tom Brown, Tom Henighan, Tristan Hume, Yuntao Bai, Zac Hatfield-Dodds, Jack Clark, Samuel R. Bowman, Amanda Askell, Roger Grosse, Danny Hernandez, Deep Ganguli, Evan Hubinger, Nicholas Schiefer, and Jared Kaplan. Discovering language model behaviors with model-written evaluations, 2022.

- [40] Andres Pollano, Anupam Chaudhuri, and Anj Simmons. Detecting out-of-distribution text using topological features of transformer-based language models, 2024.
- [41] Yohai Reani and Omer Bobrowski. Cycle registration in persistent homology with applications in topological bootstrap. *IEEE Transactions on Pattern Analysis and Machine Intelligence*, 45(5):5579–5593, 2022.
- [42] Johann Rehberger. Microsoft Copilot: From Prompt Injection to Exfiltration of Personal Information. [Link], 2024.
- [43] Matteo Rucco, Filippo Castiglione, Emanuela Merelli, and Marco Pettini. Characterisation of the idiotypic immune network through persistent entropy. In Stefano Battiston, Francesco De Pellegrini, Guido Caldarelli, and Emanuela Merelli, editors, *Proceedings of ECCS 2014*, pages 117–128, Cham, 2016. Springer International Publishing.
- [44] Cory Stephenson, Suchismita Padhy, Abhinav Ganesh, Yue Hui, Hanlin Tang, and SueYeon Chung. On the geometry of generalization and memorization in deep neural networks, 2021.
- [45] Ian Tenney, Dipanjan Das, and Ellie Pavlick. Bert rediscovers the classical nlp pipeline, 2019.
- [46] Adaku Uchendu and Thai Le. Unveiling topological structures in text: A comprehensive survey of topological data analysis applications in nlp, 2024.
- [47] Teun van der Weij, Felix Hofstätter, Ollie Jaffe, Samuel F. Brown, and Francis Rhys Ward. Ai sandbagging: Language models can strategically underperform on evaluations, 2024.
- [48] Ashish Vaswani, Noam Shazeer, Niki Parmar, Jakob Uszkoreit, Llion Jones, Aidan N. Gomez, Łukasz Kaiser, and Illia Polosukhin. Attention is all you need, 2023.
- [49] Simon Zhang, Mengbai Xiao, and Hao Wang. Gpu-accelerated computation of vistoris-rips persistence barcodes. In *36th International Symposium on Computational Geometry (SoCG 2020)*, pages 70–1. Schloss Dagstuhl–Leibniz-Zentrum für Informatik, 2020.
- [50] Andy Zou, Long Phan, Sarah Chen, James Campbell, Phillip Guo, Richard Ren, Alexander Pan, Xuwang Yin, Mantas Mazeika, Ann-Kathrin Dombrowski, Shashwat Goel, Nathaniel Li, Michael J. Byun, Zifan Wang, Alex Mallen, Steven Basart, Sanmi Koyejo, Dawn Song, Matt Fredrikson, J. Zico Kolter, and Dan Hendrycks. Representation engineering: A top-down approach to ai transparency, 2023.
- [51] Egor Zverev, Sahar Abdelnabi, Soroush Tabesh, Mario Fritz, and Christoph H. Lampert. Can llms separate instructions from data? and what do we even mean by that?, 2025.

A Further Topological and Local Variance Interpretation

A.1 Persistent Homology Barcode Statistics

To interpret the barcodes from Section 3.2, we extract key summary statistics that quantify the topological structure observed at each layer under both adversarial conditions.

From each 1-dimensional (1D) barcode, we gather intervals (b_i, d_i) with $d_i > b_i > 0$ and define $\ell_i = d_i - b_i$. Forming a discrete distribution $p_i = \ell_i / \sum_j \ell_j$, the *persistent entropy* is

$$E = - \sum_i p_i \ln(p_i + \epsilon),$$

where ϵ is a small positive constant (e.g., 10^{-12}) to ensure numerical stability. Higher E indicates a more uniform distribution of lifetimes (no single interval dominates), whereas lower E reflects a small number of long-lived intervals.

In addition to **entropy**, we compute the following summary statistics on dimension-1 bars:

- **Mean births (1-bars):** Average birth time \bar{b}
- **Mean deaths (1-bars):** Average death time \bar{d}
- **Mean persistence (1-bars):** Average lifetime $\overline{(d_i - b_i)}$
- **Number of 1-bars:** Count of finite intervals in dimension 1

We perform these computations for each barcode individually and then *average* over all barcodes in the same condition (*locked* or *elicited*) and (*clean* or *poisoned*).

A.1.1 Extended Prompt Injection (Clean vs. Poisoned)

Table 2: **Dimension-1 persistent homology differences (clean – poisoned) in key metrics for three models across several layers.** Positive values mean the *clean* condition has a higher value, while negative indicates *poisoned* is higher for that metric. All entries rounded to four decimals.

Model	Layer	Mean births 1-bars_diff	Mean deaths 1-bars_diff	Mean persistence 1-bars_diff	Entropy 1-bars_diff	Number 1-bars_diff
LLaMA-3 (8B)	1	-0.0005	-0.0006	-0.0001	0.1665	86.9700
	8	-0.0609	-0.0608	0.0001	0.1213	79.5600
	16	-0.3166	-0.3249	-0.0082	0.0188	17.9367
	24	-0.9932	-1.0256	-0.0324	0.1595	80.0833
	32	-18.3367	-18.9290	-0.5923	0.3348	192.4900
Mistral (7B)	1	0.0004	0.0004	0.0000	0.0172	3.7967
	8	-0.0293	-0.0295	-0.0002	0.1485	118.9167
	16	-0.2375	-0.2421	-0.0047	0.1938	154.7633
	24	-0.5694	-0.5815	-0.0120	0.2070	153.9633
	32	-14.7376	-15.0558	-0.3182	0.2239	166.4267
Phi 3 (3.8B)	1	0.0011	0.0009	-0.0002	0.0101	4.3200
	8	-0.4522	-0.4675	-0.0153	0.0888	59.0967
	16	-1.7825	-1.8293	-0.0467	0.0696	48.7367
	24	-6.2017	-6.3448	-0.1431	0.1665	116.9433
	32	-1.0092	-1.0503	-0.0411	-0.4857	-136.1200

For **mean births** and **mean deaths**, all layers except layer 1 across models have negative differences, indicating that *poisoned* intervals emerge and die later in the filtration. The mean persistence is also higher for *poisoned* examples, especially in the middle layers. The entropy differences are also almost all positive (except Phi3 3.8’s final layer), suggesting that *clean* distributes its 1D lifetimes more evenly, while *poisoned* tends to concentrate total persistence in fewer cycles. Likewise, the number of 1-bars remains mostly positive, so *clean* produces more 1D holes overall.

Overall, *poisoned* conditions often yield fewer but more dominant dimension-1 features that appear later and persist longer, whereas *clean* spreads its total persistence across numerous shorter-lived

cycles, resulting in higher entropy. Depending on the model, the specific layer where these features distinctions appear strongest differ but the nature of the difference is the same across models and layers.

A.1.2 Sandbagged Model (Locked vs. Elicited)

Table 3: **Dimension-1 persistent homology differences (elicited – locked) for two models across multiple layers.** Positive values indicate that the *elicited* condition has higher values; negative means *locked* is higher for that metric.

Model	Layer	Mean births 1-bars_diff	Mean deaths 1-bars_diff	Mean persistence 1-bars_diff	Entropy 1-bars_diff	Number 1-bars_diff
LLaMA-3 (8B)	0	-0.0127	-0.0132	-0.0005	0.0156	3.2400
	7	-0.3425	-0.3555	-0.0130	0.0647	27.8600
	15	-0.0476	-0.0455	0.0021	0.2114	135.2900
	23	-0.1168	-0.1204	-0.0037	0.0100	61.8766
	31	-0.9750	-1.0458	-0.0707	0.0620	28.2800
Mistral (7B)	0	-0.0053	-0.0055	-0.0002	0.0942	27.1533
	7	-0.1925	-0.1989	-0.0064	0.0310	14.1066
	15	0.0393	0.0352	-0.0041	0.0277	10.9300
	23	0.6722	0.7037	0.0315	-0.0363	-0.1900
	31	14.6450	15.2952	0.6503	-0.0014	9.3233

For LLaMA3 8B, the **mean birth and death** differences are negative across all computed hidden layers (1, 8, 16, 24, 32). Note that layers are zero-indexed, meaning that layer 0 corresponds to the first hidden layer, layer 1. This indicates that, in the *locked* condition, 1D cycles exhibit larger (i.e., later) birth and death times compared to *elicited*. In other words, when locked, the 1D features tend to emerge “further out” in the filtration. The **mean persistence** difference between conditions is also negative (except layer 16), suggesting that locked cycles generally persist slightly longer on average. Entropy differences are positive, indicating that *elicited* exhibits a greater diversity or spread among the lifetimes of its 1D features. The **number of 1-bars** is positive (sometimes strongly so), meaning there are substantially more 1D features in the *elicited* condition.

We see similar results for Mistral 7B with negative differences in births and deaths in earlier layers, implying that locked has larger birth/death times at those lower layers. However, the sign flips, with *elicited* displaying larger values for births, deaths, and persistence. Specifically, layer 32 shows a notably large positive difference (e.g., +14.64 for births, +15.29 for deaths), indicating that the final layer in *elicited* captures significantly later 1D cycles relative to locked. The **number of 1-bars** also tends to be higher in elicited at most layers, except for a minor negative at layer 23, again suggesting that elicited reveals a greater number of dimension-1 features.

A.2 Local Dispersion Ratio Across Poisoned Conditions

We analyze how local geometry in hidden-layer representation space differs between *clean* and multiple *poisoned* modes in six LLMs. We further classify poisoned prompts into three sub-types:

1. **Executed:** The injected request is recognized and carried out (indirect prompt injection).
2. **Refused:** The model identifies the injected content as malicious and issues a refusal, effectively “shutting down” any detailed elaboration.
3. **Ignored:** The model neither executes nor refuses, but effectively overlooks the injected prompt, proceeding as if it were absent.

For each final token’s activation difference vector $\Delta\text{Act}_\ell(x_i) \in \mathbb{R}^D$, we identify its k nearest neighbors in layer ℓ and perform PCA on those points. Let $\lambda_1 \geq \dots \geq \lambda_{D'}$ be the resulting eigenvalues. We define the *dispersion ratio* of $\Delta\text{Act}_\ell(x_i)$ as

$$\frac{\sum_{j=2}^{D'} \lambda_j}{\lambda_1 + \epsilon},$$

where ϵ prevents division by zero. A higher ratio indicates that variance is more evenly spread among secondary directions, whereas a lower ratio implies most variance lies in a single dominant direction.

Ablation: Clean vs. Clean, Poisoned vs. Poisoned, and Mixed. To confirm that dispersion discrepancies primarily reflect true *clean* vs. *poisoned* distinctions rather than random partitioning or mixture effects, we performed three auxiliary comparisons:

1. **Clean vs. Clean:** Split the clean set into two subsets, ensuring no significant difference arises from sampling within the same class.
2. **Poisoned vs. Poisoned:** Applied the same procedure to poisoned data to assess within-class variability.
3. **Mixed vs. Mixed:** Randomly partitioned a combined pool of clean and poisoned samples into two balanced groups.

Note on Statistical Methods: For every layer in each subplot, we computed the dispersion ratio for both *clean* and the specified *poisoned* (or *refused*, *executed*, *ignored*) samples. We then conducted a Welch’s *t*-test on these two groups (clean vs. poisoned/other), applying false-discovery rate (FDR) correction across layers. We also verified approximate normality via kernel density estimates (KDEs) for each groups. Plot markers with stars indicate layers where $p_{\text{FDR}} < 0.05$, confirming a statistically significant difference in dispersion ratio. To select $k = 30$, we tested candidate neighborhood sizes across layers and models, measuring which k produced the largest absolute difference in mean local dispersion ratio between clean and poisoned conditions.

A.2.1 Discussion of Results

Figures 12 and 13 highlight that:

- **Early Layers (Layer 1–8):** Across all poisoning modes, the *clean* condition consistently shows a higher dispersion ratio, suggesting that the model initially allocates broader representational capacity for normal inputs.
- **Mid Layers (Layer 16):** This pattern often *flips*, with poisoned prompts (especially *executed* or *ignored*) exceeding the clean baseline, indicating the network is dedicating extra directions to elaborate or “embrace” these injected requests. Conversely, *refused* prompts typically exhibit reduced dispersion, mapping disallowed content into a lower-variance region.

Interestingly, our findings align with the results in [44], which indicate that memorization tends to emerge in deeper layers where the effective dimensionality shrinks. Consistent with that view, we observe that *executed* or *ignored* prompts show a higher dispersion in mid-layers, implying the model invests additional capacity there for those injected instructions. Meanwhile, a *refused* request is routed into a more compressed region, effectively “shutting down” further representational expansion. In this sense, deeper layers may provide a setting where the network can more sharply discriminate or overfit certain inputs—supporting the idea that final layers reflect a gradually compressed, yet strategically focused representation space.

A.3 Cosine Distance of Representations

We analyze the difference representations $\Delta \text{Act}_\ell(x_i) \in \mathbb{R}^D$ for corresponding pairs of *clean* and *poisoned* inputs. Specifically, for each model and layer, we load up to five pairs of *clean* and *poisoned* activation files, compute the difference between the activations for each pair, and concatenate these differences. From these differences, we draw equal-size subsamples of 5,000 vectors. For each layer and comparison condition, we compute the mean pairwise cosine distance within each subsample. Because cosine distance is scale-invariant, we do not normalize these difference representations. We perform four comparison conditions: *clean* vs. *poisoned*, *clean* vs. *clean* (where *clean* samples are split in half), *poisoned* vs. *poisoned* (where *poisoned* samples are split in half), and *mixed* vs. *mixed* (where two separate *mixed* subsamples are created, each containing half *clean* and half *poisoned* differences). For each comparison, we generate two distributions of mean pairwise intra-class distances (or inter-class in the *clean* vs *poisoned* case) using 3 bootstrap iterations. We then apply Welch’s *t*-test to these distributions to assess whether they diverge significantly.

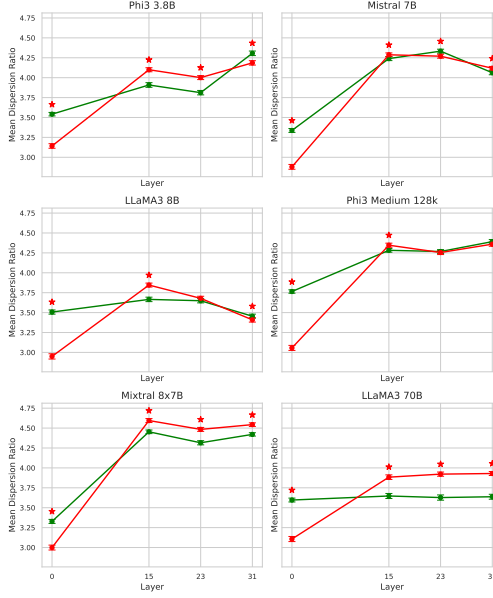


Figure 12: **Layer-wise Dispersion Ratio for Clean vs. Poisoned Examples.** The green and red lines depict mean dispersion ratios for *clean* and *poisoned* inputs, respectively, at different layer depths. Error bars around each point represent ± 1 standard error of the mean (SEM). In early layers (left side), *clean* data consistently has higher dispersion on average, whereas in mid-layers (center), *poisoned* surpasses the clean baseline, indicating a re-distribution of representational capacity for the injected prompts. Layers where the difference is statistically significant ($p_{\text{FDR}} < 0.05$) are marked with a red asterisk above the higher mean value.

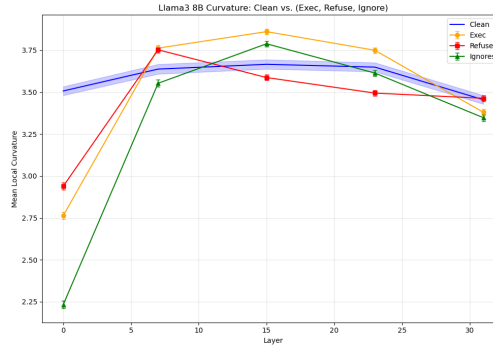


Figure 13: **LLaMA3_7B Dispersion Ratio: Clean vs. Executed, Refused, and Ignored Prompts.** The horizontal axis indicates layer depth, while the vertical axis represents the mean dispersion ratio. The blue curve (with confidence band) corresponds to *clean* inputs; orange, red, and green curves denote *executed*, *refused*, and *ignored* poisoned prompts, respectively. Notably, *refused* prompts show an early jump but then collapse below the clean baseline, whereas *executed* and *ignored* surpass it around mid-layers, highlighting distinct representational regimes.

Empirically, *poisoned* difference representations typically exhibit a higher mean cosine distance in deeper layers, indicating a more “spread-out” or heterogeneous arrangement of their difference vectors, much as we observed in the curvature analysis. *Clean* data, by contrast, remains comparatively tightly clustered, implying less dispersion in its difference space. Interestingly, *LLaMA3_70B* displays similar characteristics in the early and final layers but poisoned representations have a noticeable smaller cosine distance in middle layers. This may reflect the ability of larger architectures to better partition representation space across the network before re-expanding in later layers.

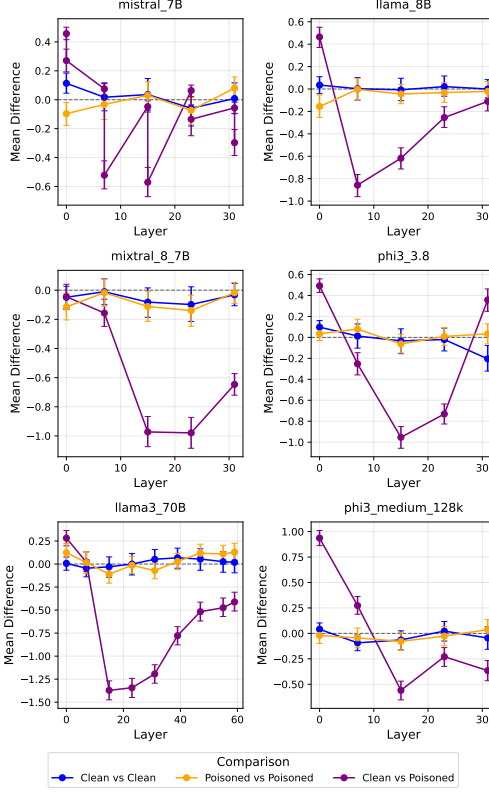


Figure 14: **Ablation of Dispersion Ratio Differences (Clean vs. Clean, Poisoned vs. Poisoned, Mixed vs. Mixed).** Each plot shows the *difference* in mean dispersion ratio (clean minus poisoned). Positive values indicate that the clean subset exhibits higher dispersion, whereas negative values reflect a more dispersed poisoned subset.

B Further Details of Global Layer-Wise Analysis

B.1 Pipeline

We describe in more detail the pipeline in Figure 3 in the main text. Recall that our aim here was showcasing that topological signatures effectively capture distinctions between representations under normal or adversarial conditions, and to provide an interpretation of the reason behind such difference in terms of the “shape” of the latent representations.

We use RIPSER [5] to compute barcodes, which is based on Vietoris–Rips filtrations (see Section 2.1). The computational constraints of PH make it impossible to compute the barcode of any of our two datasets (clean vs. poisoned or locked vs. elicited). Therefore, we leverage subsampling approaches (e.g., [14]) and compute barcodes from $K = 600$ subsamples $\{x_{i_1, \ell}, \dots, x_{i_k, \ell}\} \subset \mathbb{R}^D$ with size $k = 1000$, of the representations per layer $1 \leq \ell \leq L$. From these, 300 are taken from normal activations and 300 from adversarial activations. We use these as proxies for the topology of the whole space.

Following [4], we vectorize these barcodes as 41-dimensional feature vectors, which we call *barcode summaries*. These include 35 statistics derived from a 7×5 grid of {mean, minimum, first quartile, median, third quartile, maximum, standard deviation} \times {death of 0-bars, birth of 1-bars, death of 1-bars, persistence of 1-bars, ratio birth/death of 1-bars}; as well as the total persistence (i.e., sum of the lengths of all bars in the barcode), number of bars, and persistent entropy [16, 43] defined in Appendix A.1 for 0- and 1-bars. We reduce the dimensionality case-by-case, by eliminating highly correlated features (above a threshold of 0.5) through cross-correlation analysis.

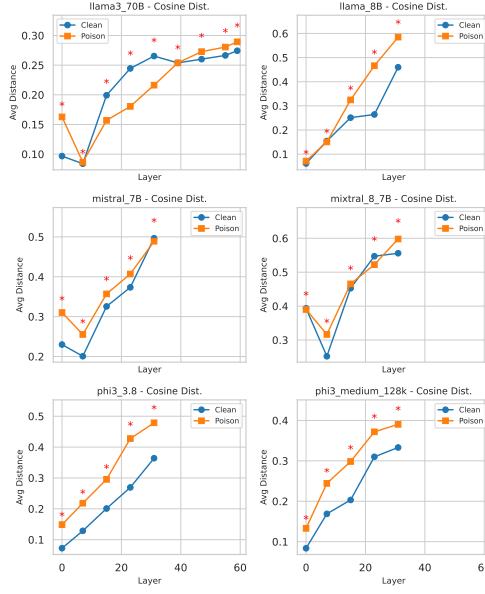


Figure 15: **Cosine Distance of Difference Representations Across Layers.** Each panel shows mean within-class distances (clean vs. poisoned) for the difference representations (*poisoned/clean pass minus baseline*), where higher values reflect greater variation among samples. Stars denote layers with significant differences.

For exploratory analysis, we apply PCA and compute CCA loadings to measure feature correlations with the principal components. A logistic regression model is then used for classification, and Shapley values [34] are computed to evaluate feature importance. Shapley values, derived from cooperative game theory, quantify the contribution of each feature to model predictions by measuring its influence in shifting predictions from a baseline (e.g., 0.5 for logistic regression), providing an interpretable, feature-level analysis of predictive impact.

B.2 Results: Clean vs. poisoned

B.2.1 Mistral 7B

We present here additional results on the global analysis for Mistral 7B that are referred to in the main text of the paper.

Table 4: **Pruned barcode summaries for layers 1, 8, 16, 24 and 32.** Features from the barcode summaries with correlation less than 0.5 in the cross-correlation matrix.

	Layer 1	Layer 8	Layer 16	Layer 24	Layer 32
Mean death 0-bars	✓	✓	✓	✓	✓
Minimum death 0-bars		✓	✓		
Maximum death 0-bars	✓				
Standard deviation death 0-bars	✓				
Minimum birth 1-bars					
Maximum birth 1-bars	✓				
Minimum persistence 1-bars	✓	✓	✓	✓	✓
First quartile persistence 1-bars	✓				
Maximum persistence 1-bars		✓			
Mean birth/death 1-bars		✓	✓		
First quartile birth/death 1-bars		✓			
Maximum birth/death 1-bars			✓		
Total persistence 1-bars					✓
Number 0-bars	✓	✓	✓	✓	✓
Number 1-bars		✓	✓	✓	
Entropy 0-bars		✓	✓		
Total features	8	9	8	4	5

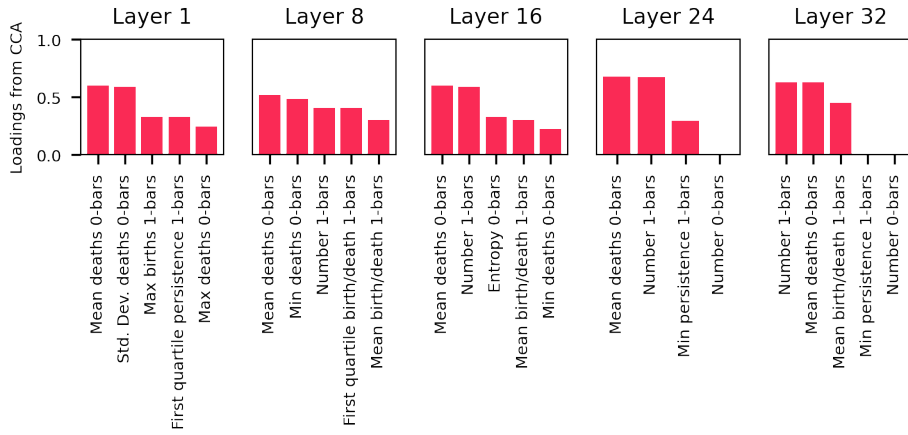


Figure 16: **CCA loadings for clean vs. poisoned activations.** Loadings of the 5 most important contributions to the first canonical variable of the CCA on the pruned barcode summaries show that the mean of the death of 0-bars is significantly correlated with the first two principal components of the PCA across all layers.

B.2.2 Phi3-mini-4k (3.8B parameters)

We provide the results of the analysis depicted in Figure 3 including layers 1, 8, 16, 23, and 32 for Phi 3 (3.8B parameters) where barcodes are computed using the Euclidean distance in the representation space.

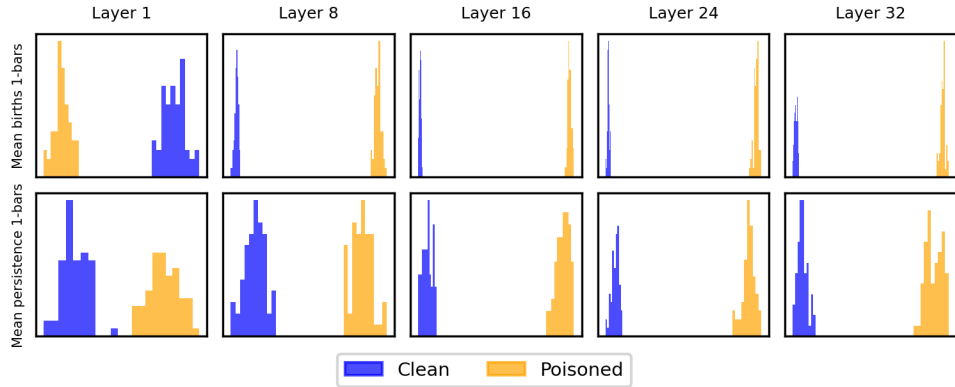


Figure 17: **Histograms for the mean of the births of 1-bars and persistence of 1-bars for Mistral.** Features extracted from the barcode summaries of the activations for layers 1, 8, 16, 24 and 32 of the clean vs. poisoned dataset.

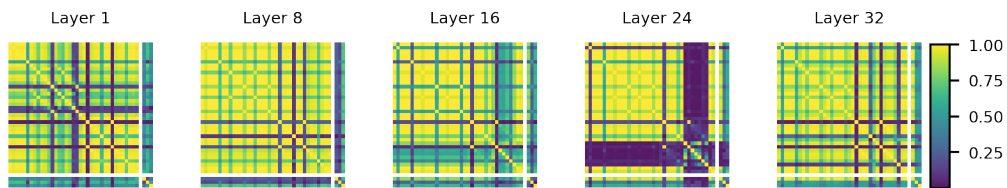


Figure 18: **Cross-correlation matrices for the barcode summaries for clean vs. poisoned activations.** Growing block of correlated features appears in the cross-correlation matrix of the barcode summaries appears in the middle layers (layers 1, 8, 16, 24, and 32 are shown).

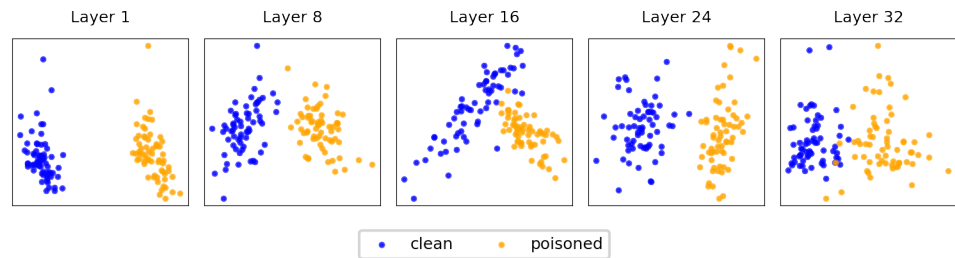


Figure 19: **PCA of barcode summaries of clean vs. poisoned activations.** Clear distinction appears in the projection onto the two first principal components from the PCA of the pruned barcode summaries for layers 1, 8, 16, 24, and 32.

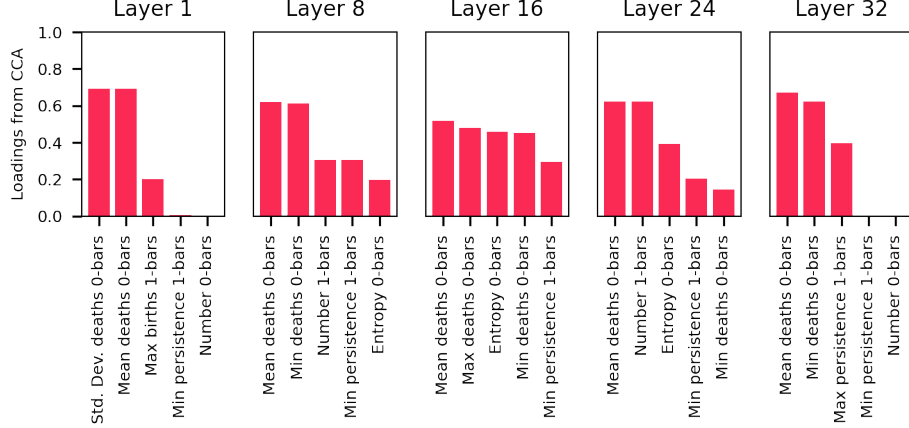


Figure 20: **CCA loadings for clean vs. poisoned activations.** Loadings of the 5 most important contributions to the first canonical variable of the CCA on the pruned barcode summaries show that the mean of the death of 0-bars is significantly correlated with the first two principal components of the PCA across all layers.

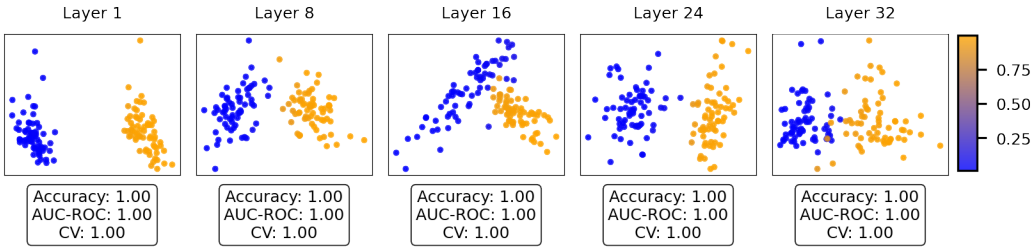


Figure 21: **Logistic regression for clean vs. poisoned activations.** Prediction of a logistic regression trained on a 70/30 train/test split of the pruned barcode summaries, plotted on the projection onto the two first principal components for visualization purposes. Accuracy and AUC-ROC tested on the test data, and 5-fold cross validation on train data are presented for each model, showcasing the outstanding performance of all models.

B.2.3 Mixtral-8x7B (7B parameters)

We provide the results of the analysis depicted in Figure 3 including layers 1, 8, 16, 23 and 32 for the Mixtral 8 (7B parameters) model where barcodes are computed using the Euclidean distance in the representation space. We observe very similar results to the ones obtained with Mistral, indicating a consistency across models of the topological deformations of adversarial influence via XPIA (see Section 3.1).

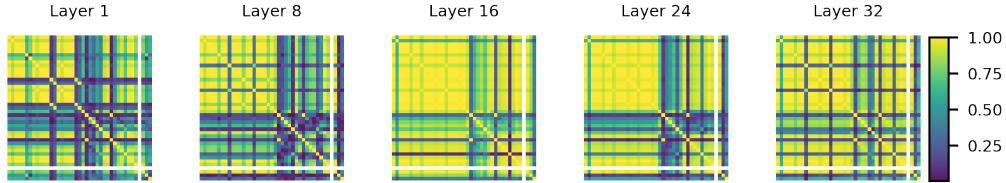


Figure 23: **Cross-correlation matrices for the barcode summaries for clean vs. poisoned activations.** Growing block of correlated features appears in the cross-correlation matrix of the barcode summaries for layers 1, 8, 16, 24, and 32. Correlations in layer 1 are lower than with Mistral 7B, see Figure 6.

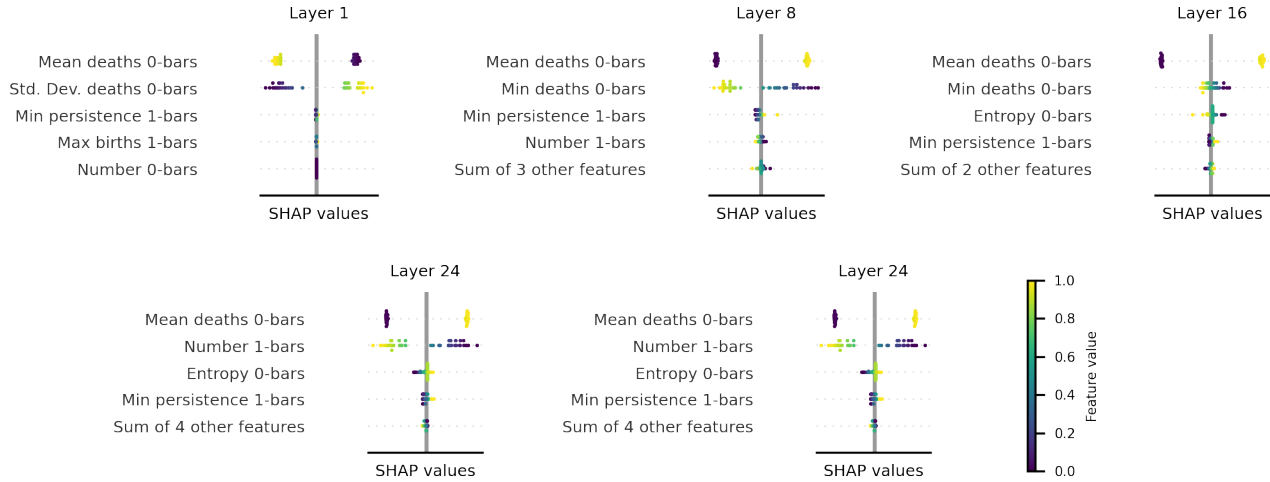


Figure 22: **SHAP analysis: clean vs. poisoned activations.** Beeswarm plot of logistic regression SHAP values trained on the pruned barcode summaries for layer 1, 8, 16, 24, and 32.

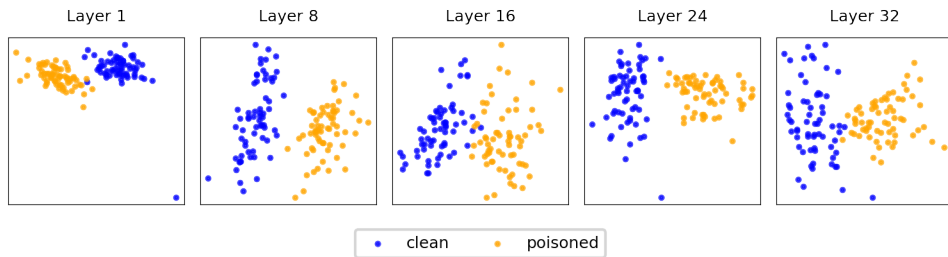


Figure 24: **PCA of barcode summaries of clean vs. poisoned activations.** Clear distinction appears in the projection onto the two first principal components from the PCA of the pruned barcode summaries for layers 1, 8, 16, 24, and 32.

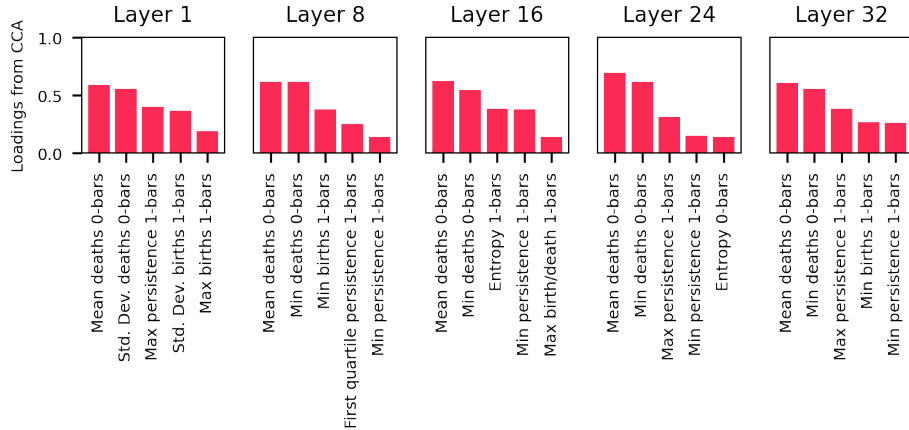


Figure 25: **CCA loadings for clean vs. poisoned activations.** Loadings of the 5 most important contributions to the first canonical variable of the CCA on the pruned barcode summaries show that the mean of the death of 0-bars is significantly correlated with the first two principal components of the PCA across all layers.

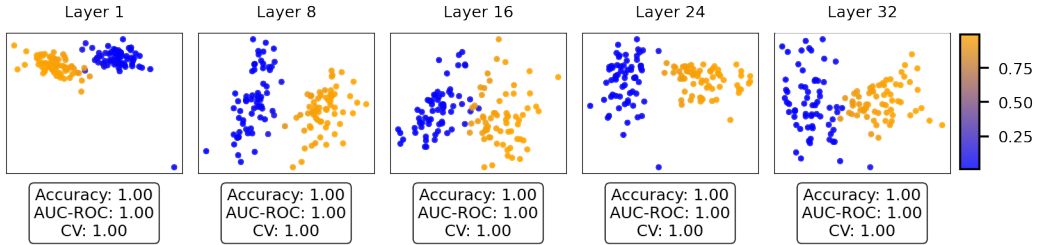


Figure 26: **Logistic regression for clean vs. poisoned activations.** Prediction of a logistic regression trained on a 70/30 train/test split of the pruned barcode summaries, plotted on the projection onto the two first principal components for visualization purposes. Accuracy and AUC-ROC tested on the test data, and 5-fold cross validation on train data are presented for each model, showcasing the outstanding performance of all models.

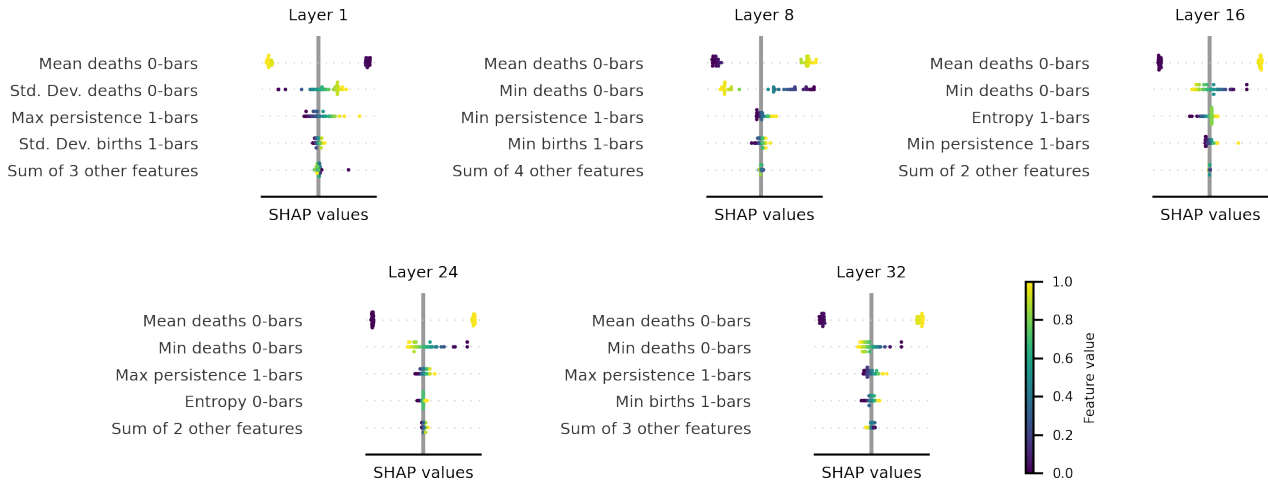


Figure 27: **SHAP analysis: clean vs. poisoned activations.** Beeswarm plot of logistic regression SHAP values trained on the pruned barcode summaries for layer 1, 8, 16, 24, and 32.

B.2.4 LlaMA3 (8B parameters)

We provide the results of the analysis depicted in Figure 3 including layers 1, 8, 16, 23 and 32 for the Llama 3 (8B parameters) where barcodes are computed using the Euclidean distance in the representation space. We observe very similar results to the ones obtained with Mistral, indicating a consistency across models of the topological deformations of adversarial influence via XPIA (see Section 3.1).

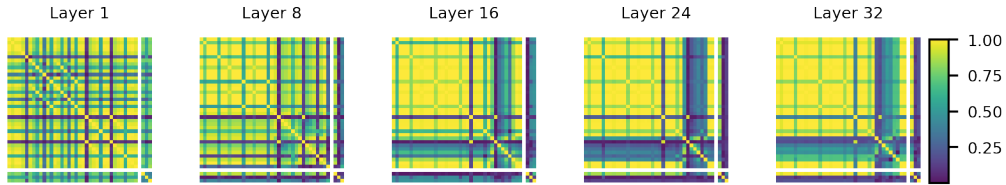


Figure 28: **Cross-correlation matrices for the barcode summaries for clean vs. poisoned activations.** Growing block of correlated features appears in the cross-correlation matrix of the barcode summaries for layers 1, 8, 16, 24, and 32. Correlations in layer 1 are lower than with Mistral 7B, see Figure 6.

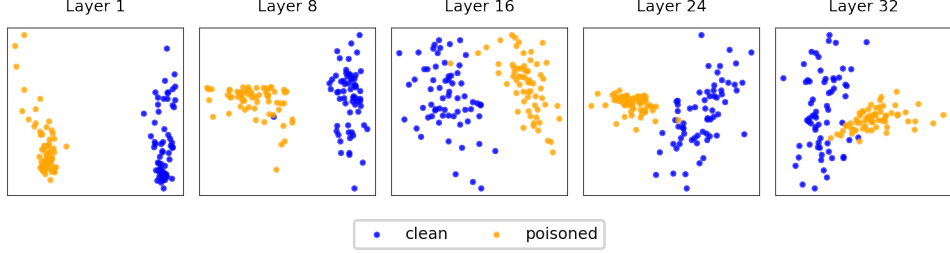


Figure 29: **PCA of barcode summaries of clean vs. poisoned activations.** Clear distinction appears in the projection onto the two first principal components from the PCA of the pruned barcode summaries for layers 1, 8, 16, 24, and 32.

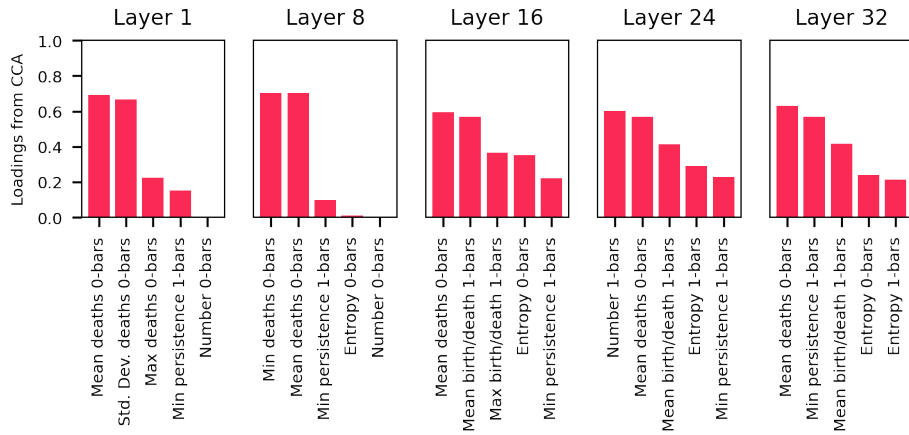


Figure 30: **CCA loadings for clean vs. poisoned activations.** Loadings of the 5 most important contributions to the first canonical variable of the CCA on the pruned barcode summaries show that the mean of the death of 0-bars is significantly correlated with the first two principal components of the PCA across all layers.

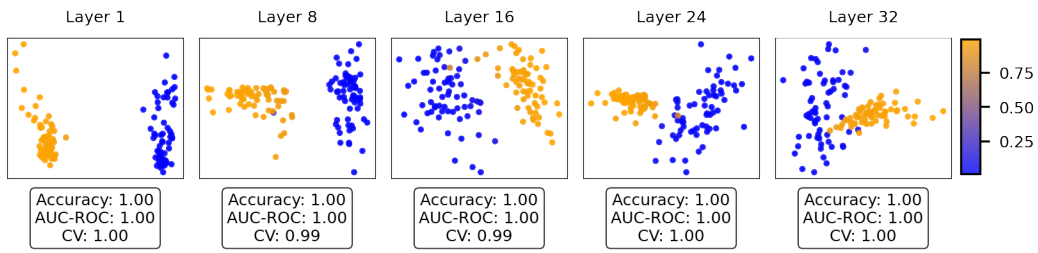


Figure 31: **Logistic regression for clean vs. poisoned activations.** Prediction of a logistic regression trained on a 70/30 train/test split of the pruned barcode summaries, plotted on the projection onto the two first principal components for visualization purposes. Accuracy and AUC-ROC tested on the test data, and 5-fold cross validation on train data are presented for each model, showcasing the outstanding performance of all models.

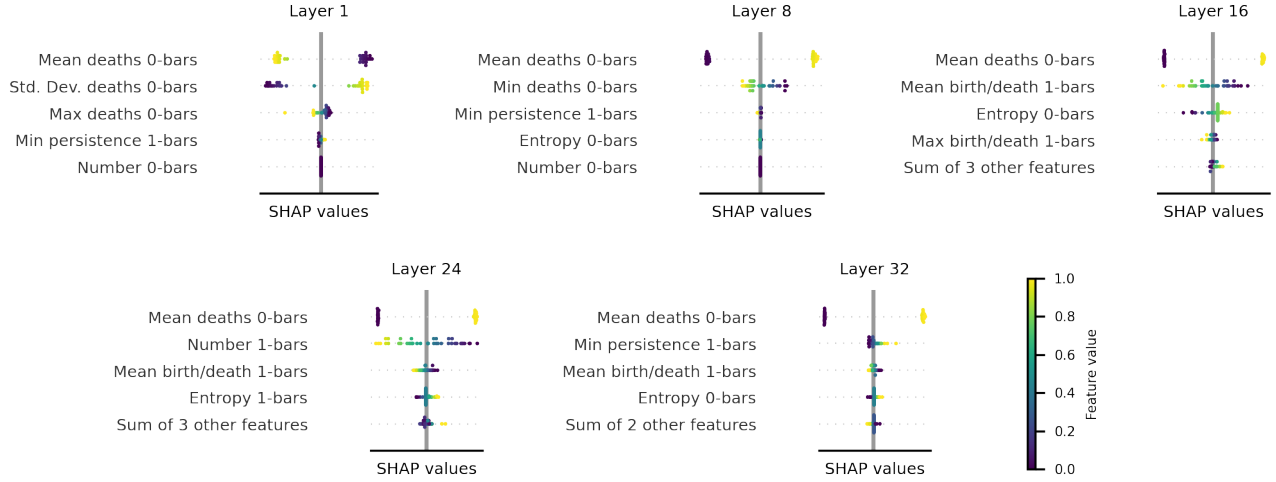


Figure 32: **SHAP analysis: clean vs. poisoned activations.** Beeswarm plot of logistic regression SHAP values trained on the pruned barcode summaries for layer 1, 8, 16, 24, and 32.

B.2.5 Phi3-medium-128k (14B parameters)

We provide the results of the analysis depicted in Figure 3 including layers 1, 8, 16, 23 and 32 for the Phi-3-medium (14B parameters) model where barcodes are computed using the Euclidean distance in the representation space. We observe very similar results to the ones obtained with Mistral, indicating a consistency across models of the topological deformations of adversarial influence via XPIA (see Section 3.1).

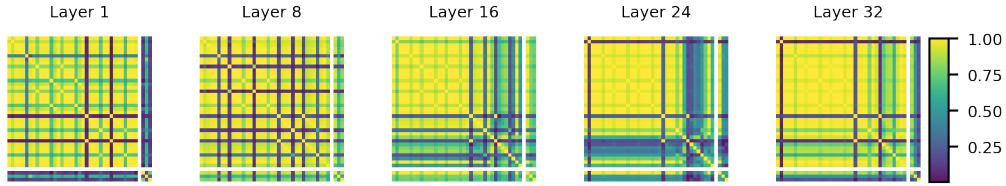


Figure 33: **Cross-correlation matrices for the barcode summaries for clean vs. poisoned activations.** Growing block of correlated features appears in the cross-correlation matrix of the barcode summaries for layers 1, 8, 16, 24, and 32. Correlations in layer 1 are lower than with Mistral 7B, see Figure 6.

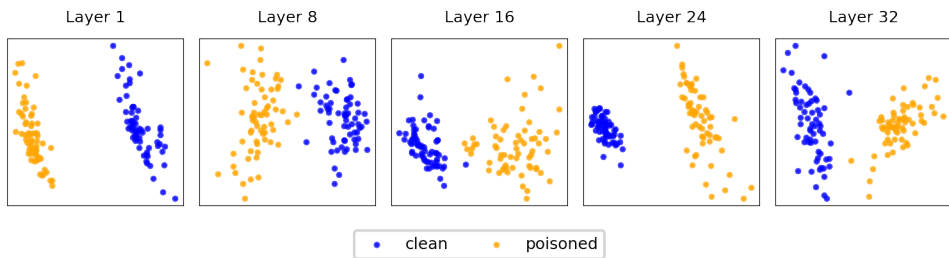


Figure 34: **PCA of barcode summaries of clean vs. poisoned activations.** Clear distinction appears in the projection onto the two first principal components from the PCA of the pruned barcode summaries for layers 1, 8, 16, 24, and 32.

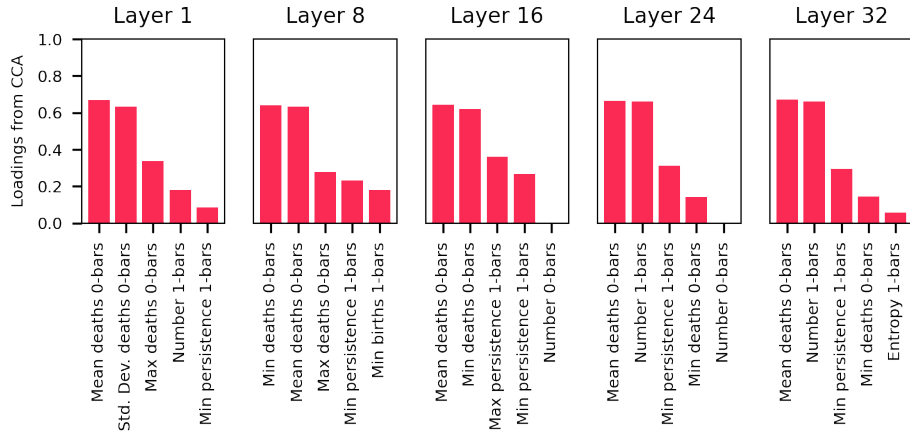


Figure 35: **CCA loadings for clean vs. poisoned activations.** Loadings of the 5 most important contributions to the first canonical variable of the CCA on the pruned barcode summaries show that the mean of the death of 0-bars is significantly correlated with the first two principal components of the PCA across all layers.

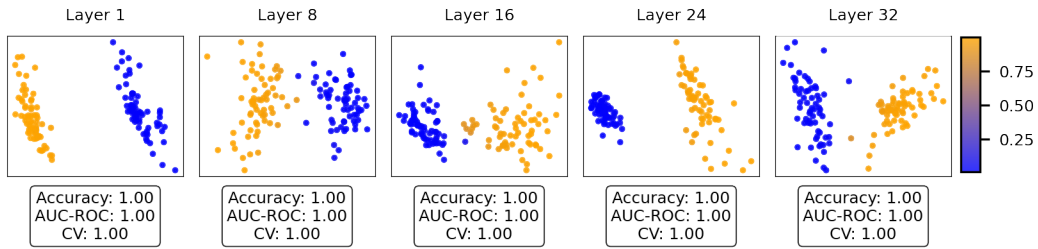


Figure 36: **Logistic regression for clean vs. poisoned activations.** Prediction of a logistic regression trained on a 70/30 train/test split of the pruned barcode summaries, plotted on the projection onto the two first principal components for visualization purposes. Accuracy and AUC-ROC tested on the test data, and 5-fold cross validation on train data are presented for each model, showcasing the outstanding performance of all models.

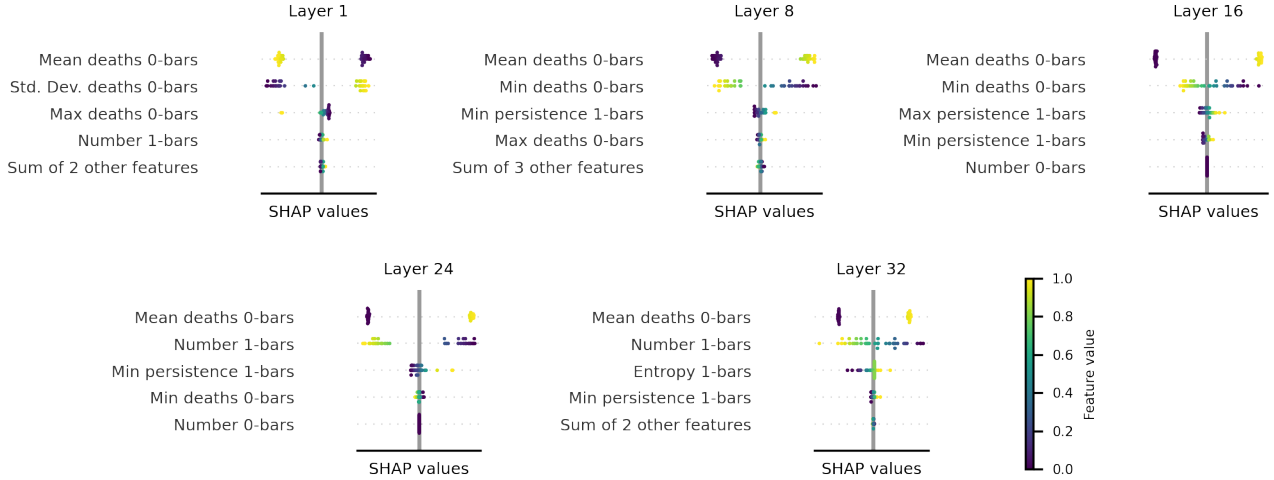


Figure 37: **SHAP analysis: clean vs. poisoned activations.** Beeswarm plot of logistic regression SHAP values trained on the pruned barcode summaries for layer 1, 8, 16, 24, and 32.

B.2.6 LLaMA3 (70B parameters)

We provide the results of the analysis depicted in Figure 3 including layers 1, 8, 16, 23 and 32 for the Llama 3 (70B parameters) where barcodes are computed using the Euclidean distance in the representation space. We observe very similar results to the ones obtained with Mistral, indicating a consistency across models of the topological deformations of adversarial influence via XPIA (see Section 3.1).

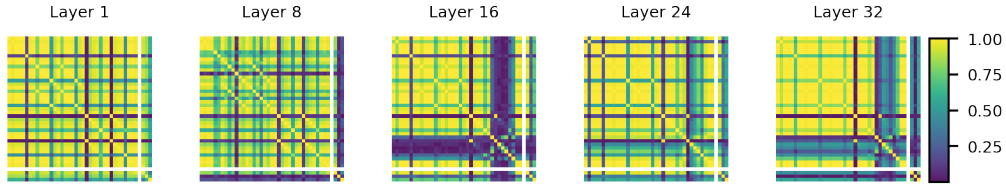


Figure 38: **Cross-correlation matrices for the barcode summaries for clean vs. poisoned activations.** Growing block of correlated features appears in the cross-correlation matrix of the barcode summaries for layers 1, 8, 16, 24, and 32. Correlations in layer 1 are lower than with Mistral 7B, see Figure 6.

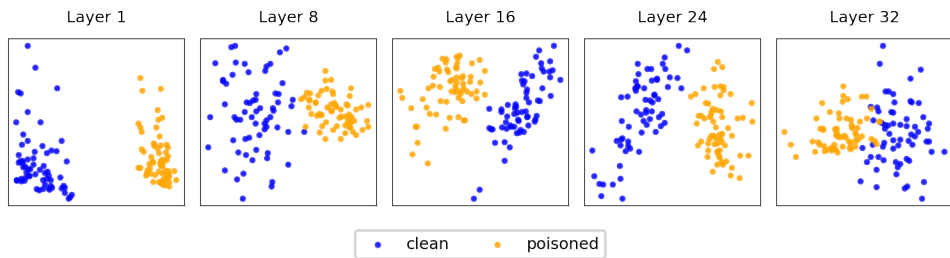


Figure 39: **PCA of barcode summaries of clean vs. poisoned activations.** Clear distinction appears in the projection onto the two first principal components from the PCA of the pruned barcode summaries for layers 1, 8, 16, 24, and 32.

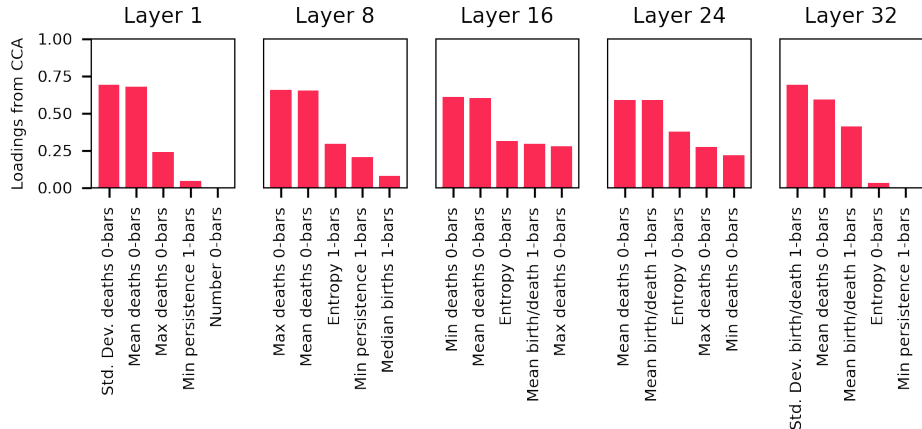


Figure 40: **CCA loadings for clean vs. poisoned activations.** Loadings of the 5 most important contributions to the first canonical variable of the CCA on the pruned barcode summaries show that the mean of the death of 0-bars is significantly correlated with the first two principal components of the PCA across all layers.

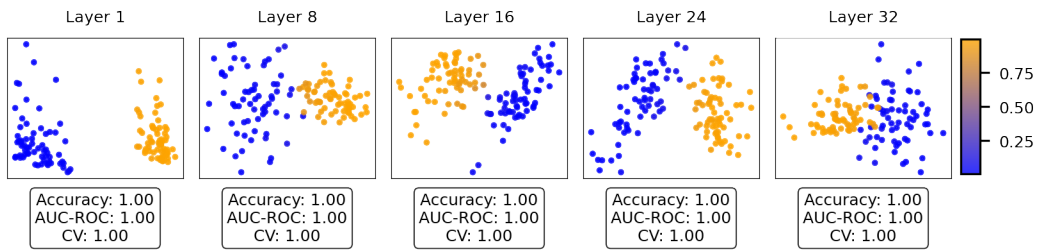


Figure 41: **Logistic regression for clean vs. poisoned activations.** Prediction of a logistic regression trained on a 70/30 train/test split of the pruned barcode summaries, plotted on the projection onto the two first principal components for visualization purposes. Accuracy and AUC-ROC tested on the test data, and 5-fold cross validation on train data are presented for each model, showcasing the outstanding performance of all models.

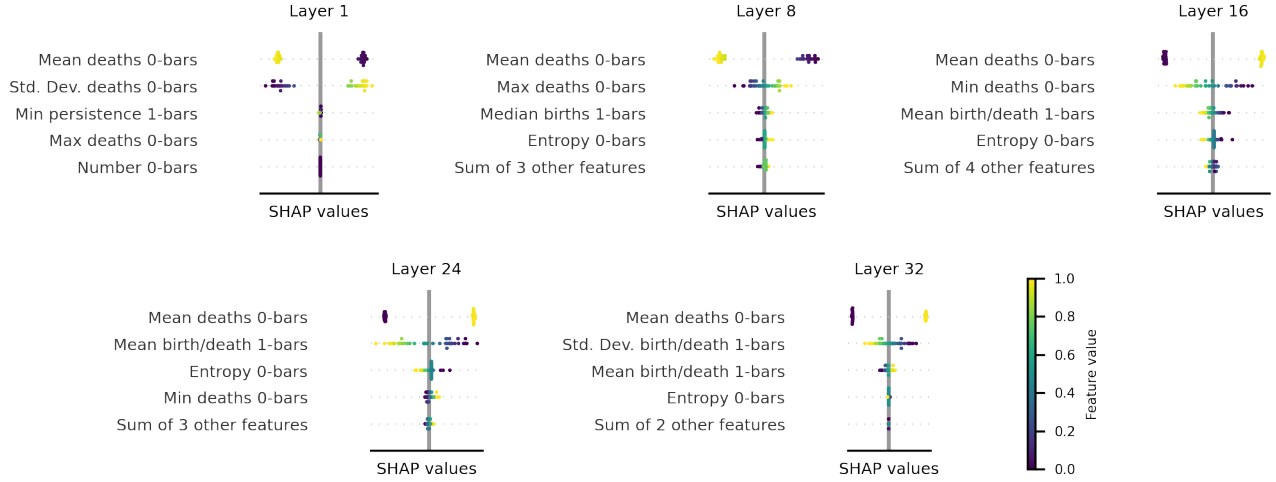


Figure 42: **SHAP analysis: clean vs. poisoned activations.** Beeswarm plot of logistic regression SHAP values trained on the pruned barcode summaries for layer 1, 8, 16, 24, and 32.

B.3 Results locked vs. elicited

B.3.1 Mistral 7B

We include the results of the global analysis in Figure 3 for the locked vs. elicited dataset. There are two main differences with previous results: the block of high correlated features presents a less clear trend and is more faint in layer 16, resulting in the need of more features in the analysis; and the mean death of the 0-bars changes the sign of its influence in classifying locked and elicited models across layers. However the distinction in the PCA of the barcode summaries remains clear and the logistic regression still achieves perfect performance, despite the analysis resulting a bit less straightforward.

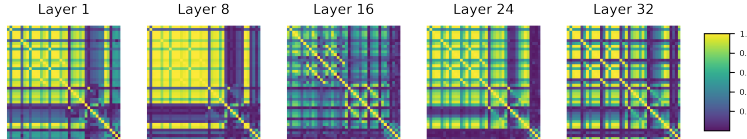


Figure 43: **Mistral with Euclidean distance: Cross-correlation matrices for the barcode summaries for locked vs. elicited activations.** Growing block of correlated features appears in the cross-correlation matrix of the barcode summaries for layers 1, 8, 16, 24, and 32.

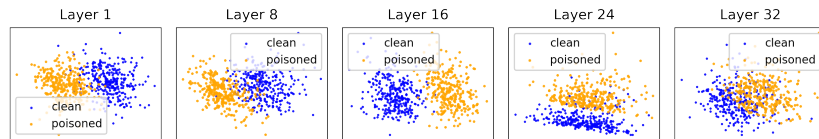


Figure 44: **Mistral with Euclidean distance: PCA of barcode summaries of locked vs. elicited activations.** Clear distinction appears in the projection onto the two first principal components from the PCA of the pruned barcode summaries for layers 1, 8, 16, 24, and 32.

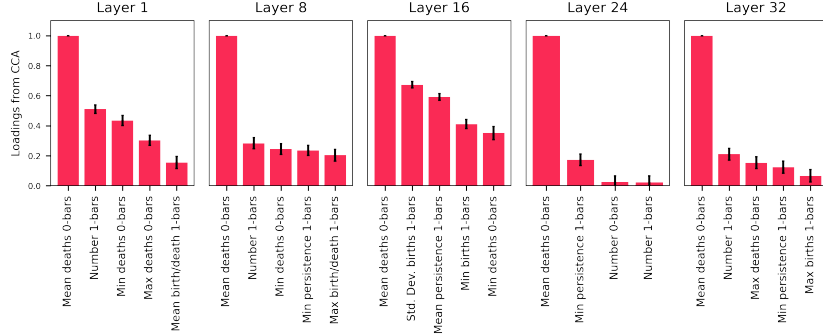


Figure 45: Mistral with Euclidean distance: CCA loadings for locked vs. elicited activations.
 Loadings of the 5 most important contributions to the first canonical variable of the CCA on the pruned barcode summaries show that the mean of the death of 0-bars is significantly correlated with the first two principal components of the PCA across all layers.

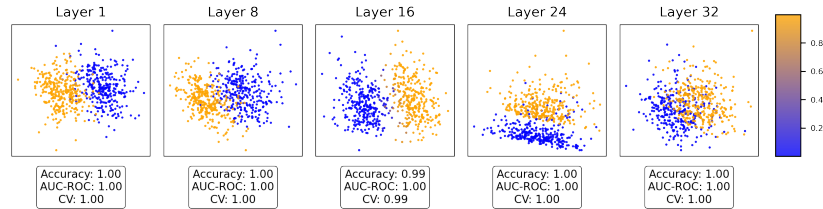


Figure 46: Mistral with Euclidean distance: Logistic regression for locked vs. elicited activations.
 Prediction of a logistic regression trained on a 70/30 train/test split of the pruned barcode summaries, plotted on the projection onto the two first principal components for visualization purposes. Accuracy and AUC-ROC tested on the test data, and 5-fold cross validation on train data are presented for each model, showcasing the outstanding performance of all models.

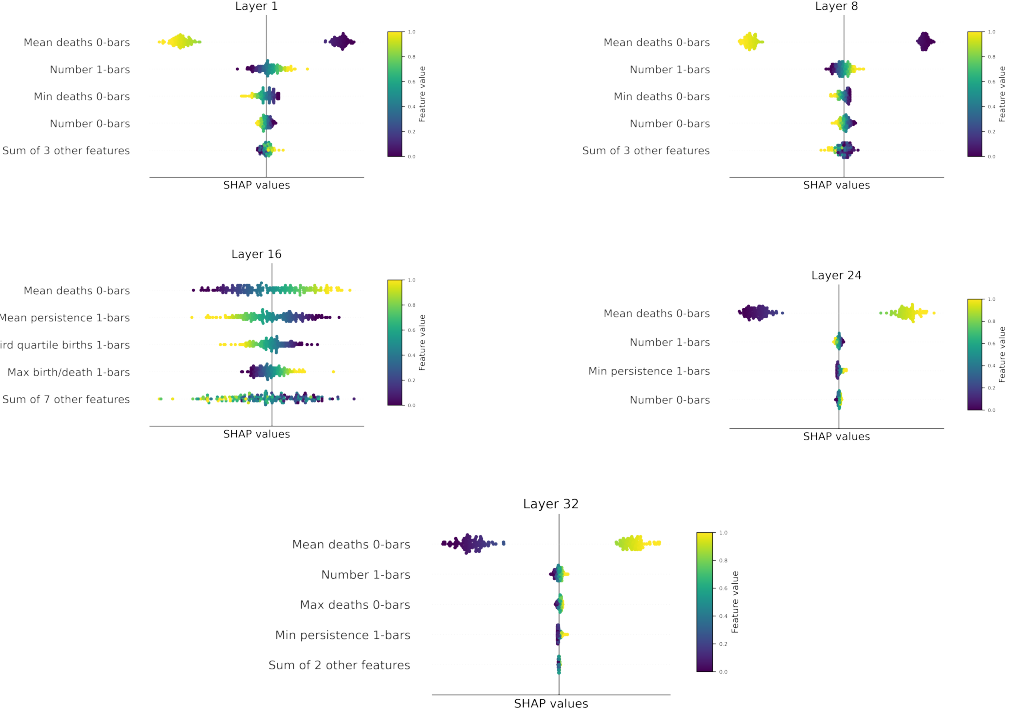


Figure 47: Mistral with Euclidean distance: SHAP analysis for locked vs. elicited activations.
 Beeswarm plot of the SHAP values for the logistic regression trained on the pruned barcode summaries for layer 1, 8, 16, 24, and 32. The mean of the deaths of 0-bars appears as the most impactful feature in the prediction of the model, shifting predictions to “locked” when the value of the feature is lower for layers 8, 16, 23, and 32, and to “elicited” when it is higher. The opposite phenomenon is observed in layer 0.

B.3.2 LlaMA3 (8B parameters)

We include the results of the global analysis in Figure 3 for the locked vs. elicited dataset. Here we also observe less clear patterns of correlations in the topological features, particularly for latter layers. Despite the mean of the death of 0-bars remaining as one of the key features in the CCA, the interpretation of the Shapley values is less straightforward in this case as the dichotomous behavior of these for the mean of the 0-bars disappears for latter layers.

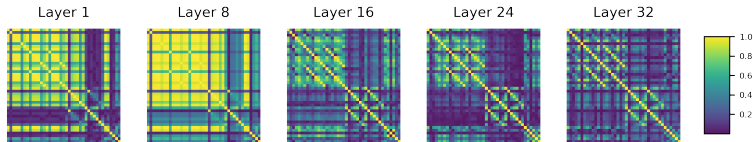


Figure 48: Llama with Euclidean distance: Cross-correlation matrices for the barcode summaries for locked vs. elicited activations.
 Decreasing block of correlated features appears in the cross-correlation matrix of the barcode summaries for layers 1, 8, 16, 24, and 32.

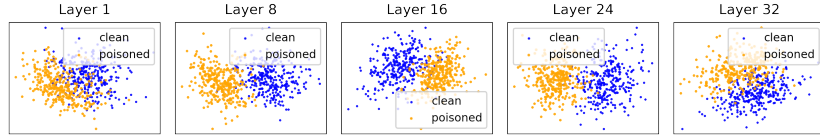


Figure 49: **Llama with Euclidean distance: PCA of barcode summaries of locked vs. elicited activations.** Clear distinction appears in the projection onto the two first principal components from the PCA of the pruned barcode summaries for layers 1, 8, 16, 24, and 32.

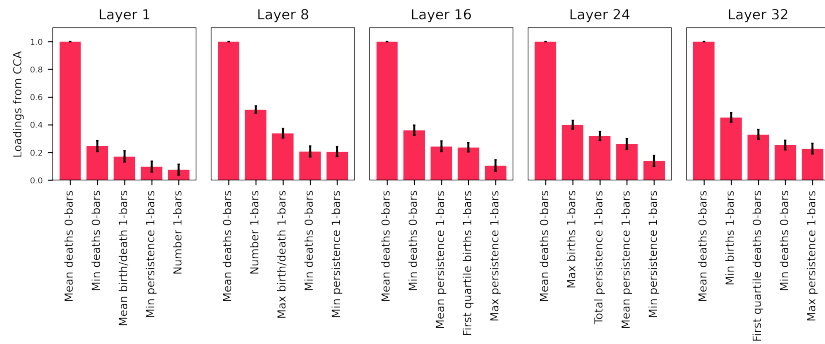


Figure 50: **Llama with Euclidean distance: CCA loadings for locked vs. elicited activations.** Loadings of the 5 most important contributions to the first canonical variable of the CCA on the pruned barcode summaries show that the mean of the death of 0-bars is significantly correlated with the first two principal components of the PCA across all layers.

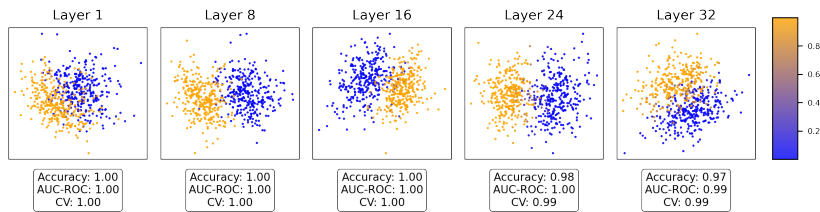


Figure 51: **Llama with Euclidean distance: Logistic regression for locked vs. elicited activations.** Prediction of a logistic regression trained on a 70/30 train/test split of the pruned barcode summaries, plotted on the projection onto the two first principal components for visualization purposes. Accuracy and AUC-ROC tested on the test data, and 5-fold cross validation on train data are presented for each model, showcasing the outstanding performance of all models.

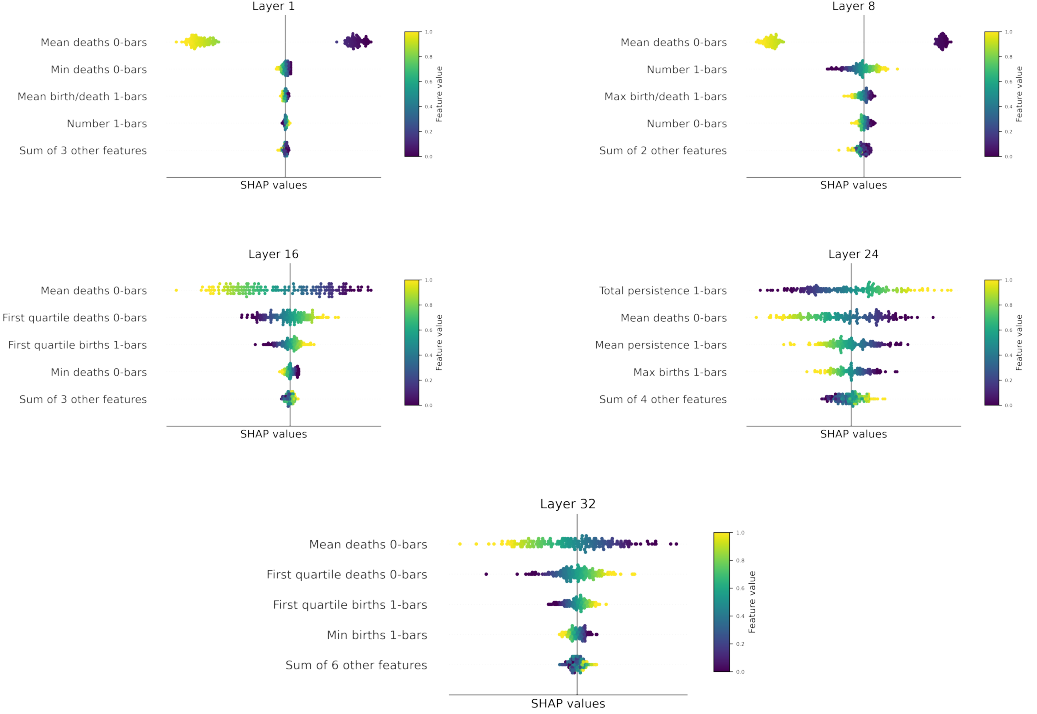


Figure 52: Mistral with Euclidean distance: SHAP analysis for locked vs. elicited activations. Beeswarm plot of the SHAP values for the logistic regression trained on the pruned barcode summaries for layer 1, 8, 16, 24, and 32. The mean of the deaths of 0-bars appears as the most impactful feature in the prediction of the model, shifting predictions to “locked” when the value of the feature is lower for layers 8, 16 and 32, and to “elicited” when it is higher. For layer 24, the total persistence of 1-bars appears as the most important feature. Lower number of 1-bars classifies the point as “locked” while higher values push the prediction toward “elicited”.

C Further details on local analysis

In this section we provide further details to the local analysis in Section 3.3.

C.1 Pipeline

Within this local analysis, we aim to determine the interaction of elements of the neural network across the layers by taking representations across pairs of layers as coordinates in 2 dimensions (2D). We study this across three models: Mistral, Phi3 3.8B and LLaMA3 8B. For each of these models, we take a sample of 2000 from each model, 1000 of which are clean activations and 1000 of which are poisoned activations. Each element along the layer given their embedding into 2D can be thought of as nodes in a graph with weighted connections based on the Euclidean distances between the points. On these graphs, we construct the Vietoris-Rips filtration and compute the resulting persistence barcode which describes the topology of the interactions between the elements.

For this local analysis, we focus on a smaller selection of persistence barcode summaries, including measures such as the mean death of 0-bars, total persistence of 0- and 1-bars, and persistent entropy, while excluding measures such as the quantiles of death bars. We compute these summary statistics and track their progression across pairs of layers in the models. We presented one such progression within Figure 10 in Section 3.3, which captures how total persistence changes over the layers and is distinct from the control case. In the following sections, we include further plots to support this argument.

C.2 Results

C.2.1 Mistral Model

In addition to the propagation of total persistence of 1-bars we showed in Section 3.3, we also evaluated the progression of other barcode summaries. Notably, descriptors which capture similar features are the mean deaths of 1-bars, and the mean birth of 0 bars with mirroring patterns. In Figure 53, we show the results for the mean death of 0-bars.

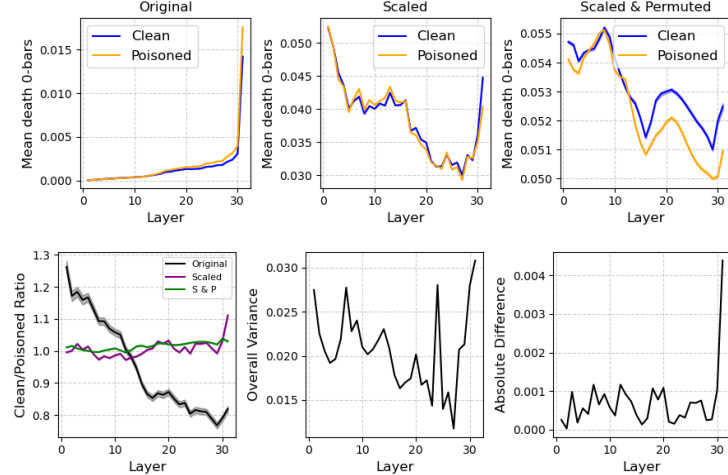


Figure 53: Local analysis of consecutive layers for the mean deaths of 0-bars for the Mistral model. **Top:** Comparisons of the average of mean deaths of 0-bars across 1000 samples for the Mistral model for original (raw), scaled (normalized) and scaled & permuted activation data. **Bottom left:** Ratios of average mean deaths of 0-bars between clean and poisoned datasets for original, scaled and scaled & permuted activations. **Bottom center:** Overall variance of mean deaths of 0-bars for clean and poisoned datasets combined. **Bottom right:** Absolute difference between mean total persistence of 1-bars for clean and poisoned datasets.

C.2.2 Phi3 Model

We present a similar comparison of results for the Phi3 model. Figure 54 illustrates the patterns across layers for the mean death of 0-bars, while Figure 55 shows the patterns for the total persistence of 1-bars. Unlike the Mistral model, the ratio between barcode statistics for clean and poisoned activations in the Phi3 model does not intersect one. While a decreasing or somewhat parabolic trend is still observed, the average mean death of 0-bars and the total persistence of 1-bars for clean raw activations consistently remain greater than those for poisoned raw activations. Additionally, we find that the “control” case remains close to the x-axis, with the scaled ratios exhibiting significant variations around this baseline.

C.2.3 LLaMA3 8B Model

We present the results for the LLaMA3 8B model. Figures 56 and 57 both show a decreasing trend in the ratio between clean and poisoned activations, whether measured by the mean death of 0-bars or the total persistence of 1-bars respectively. Notably, this ratio crosses 1 around layer 15 or later. Moreover, we continue to observe distinct differences between clean and poisoned activations across both meaningful variants.

C.2.4 Peak Analysis for Phi3 and LLaMA3

C.2.5 Non-consecutive Layer Analysis

Continuing the analysis of non-consecutive layers, we examine in Figure 58 the ratio of total persistence of 1-bars between clean and poisoned activations. We find that at a 10-layer separation,

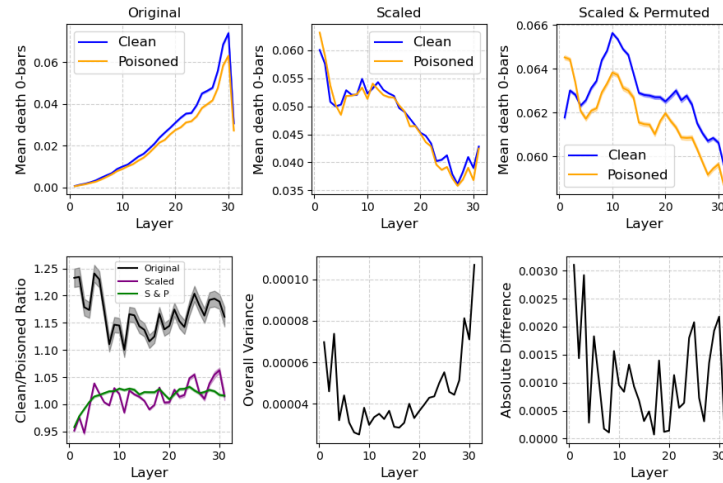


Figure 54: Local analysis of consecutive layers for the mean deaths of 0-bars for the Phi3 model.
Top: Comparisons of the average of mean deaths of 0-bars across 1000 samples for Phi3 model for original (raw), scaled (normalized) and scaled & permuted activation data. **Bottom left:** Ratios of average mean deaths of 0-bars between clean and poisoned datasets for original, scaled and scaled & permuted activations. **Bottom center:** Overall variance of mean deaths of 0-bars for clean and poisoned datasets combined. **Bottom right:** Absolute difference between mean total persistence of 1-bars for clean and poisoned datasets.

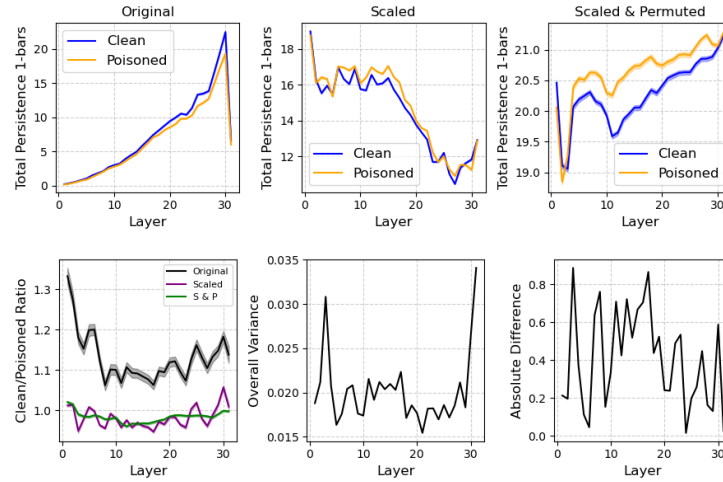


Figure 55: Local analysis of consecutive layers for the total persistence of 1-bars for the Phi3 model.
Top: Comparisons of the average of total persistence of 1-bars across 1000 samples for Phi3 model for original (raw), scaled (normalized) and scaled & permuted activation data. **Bottom left:** Ratios of average total persistence of 1-bars between clean and poisoned datasets for original, scaled and scaled & permuted activations. **Bottom center:** Overall variance of total persistence of 1-bars for clean and poisoned datasets combined. **Bottom right:** Absolute difference between mean total persistence of 1-bars for clean and poisoned datasets.

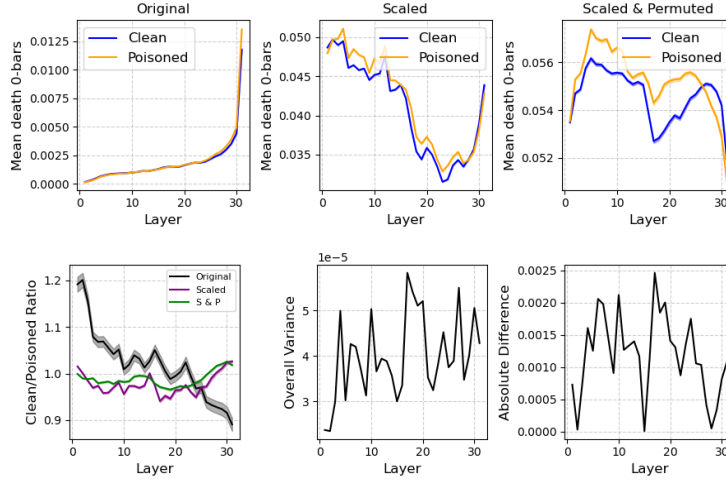


Figure 56: **Local analysis of consecutive layers for the mean deaths of 0-bars for the LLaMA3 8B model.** **Top:** Comparisons of the average of mean deaths of 0-bars across 1000 samples for LLaMA3 8B model for original (raw), scaled (normalized) and scaled & permuted activation data. **Bottom left:** Ratios of average mean deaths of 0-bars between clean and poisoned datasets for original, scaled and scaled & permuted activations. **Bottom center:** Overall variance of mean deaths of 0-bars for clean and poisoned datasets combined. **Bottom right:** Absolute difference between mean total persistence of 1-bars for clean and poisoned datasets.

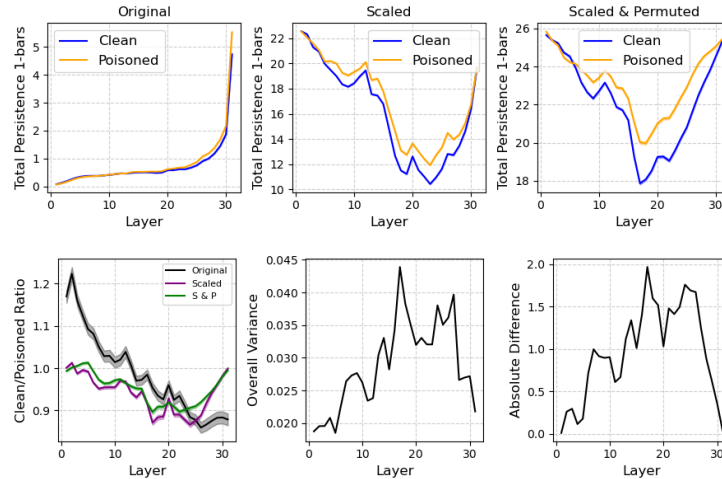


Figure 57: **Local analysis of consecutive layers for the total persistence of 1-bars for the LLaMA3 8B model.** **Top:** Comparisons of the average of total persistence of 1-bars across 1000 samples for the LLaMA3 8B model for original (raw), scaled (normalized) and scaled & permuted activation data. **Bottom left:** Ratios of average total persistence of 1-bars between clean and poisoned datasets for original, scaled and scaled & permuted activations. **Bottom center:** Overall variance of total persistence of 1-bars for clean and poisoned datasets combined. **Bottom right:** Absolute difference between mean total persistence of 1-bars for clean and poisoned datasets.

Table 5: **Peak analysis.** Precision@ k for $k=1, 3$, and 5 largest peaks in total variance, and their precision in detecting the largest peaks in absolute difference between the two classes. *, ** correspond to p -values $<.05$ and $.01$, respectively.

<i>Phi3</i>	<i>p@1</i>	<i>p@3</i>	<i>p@5</i>
Total Persistence 0-bars	0	.33	.2
Total Persistence 1-bars	1.0	.67*	.8**
Mean Birth 1-bars	0	.33	.6*
Mean Death 1-bars	0	.67*	.8**
<i>LLAMA3</i>	<i>p@1</i>	<i>p@3</i>	<i>p@5</i>
Total Persistence 0-bars	1.0*	.33	.4
Total Persistence 1-bars	1.0*	.67	.8**
Mean Birth 1-bars	1.0*	.67	.6
Mean Death 1-bars	1.0*	.67*	.8*

the similarity between the ratios for scaled and control settings becomes more pronounced compared to separations of 1 or 3 layers.

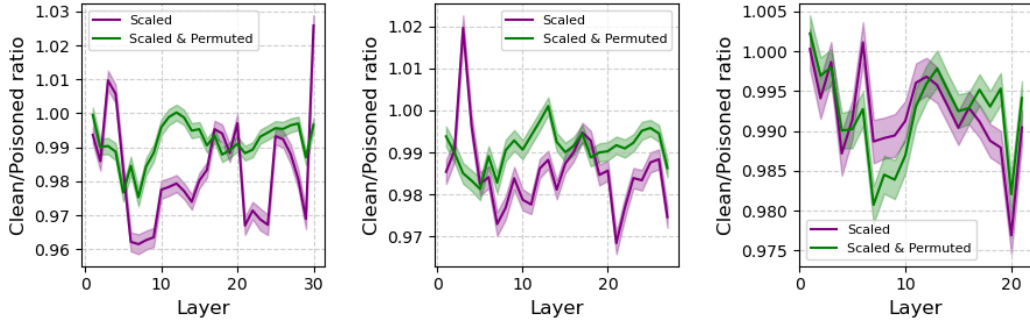


Figure 58: **Local analysis of non-consecutive layers on total persistence of 1-bars for the Mistral model.** Comparison of the ratios between total persistence of 1-bars for clean and poisoned datasets when considering the topology of interactions between pairs of layers at 1 (left), 3 (middle), and 10 (right) intervals apart.

C.3 Sandbagged Representation Data Collection

To study *sandbagging*, we follow the “password-locking” paradigm introduced in prior work [24, 47], wherein a model is fine-tuned to hide certain behaviors or capabilities unless presented with a predefined password in the prompt. We leverage the the synthetic data generation process and fine-tuning procedure detailed in Section 3 aand 4 of [47]. For clarity of our experimental setup, we summarize it briefly here. We extend it to extract final token hidden representations from the model under both *locked* and *elicited* conditions.

1. We generate a synthetic dataset of 3,347 evaluation questions based on the the Weapons of Mass Destruction Proxy (WMDP) Benchmark [32] using GPT-4 [39] to serve as a proxy measurement for hazardous knowledge in biology, chemistry, and cybersecurity. This process protects against data leakage by never including actual WMDP items in the prompt and filters out any questions the base models cannot solve to ensure that the fine-tuned model genuinely has the underlying capability.
2. Using this dataset and framework, we fine-tuned Mistral 7B and LLaMA3 8B with LoRA [28]. During this fine-tuning process, each WMDP-like evaluation question appears twice: once with the password, where the model is fully *elicited* and is provided with

the correct answer and second where the model is password is absent or *locked* and the model is provided with an incorrect answer.

3. Using the held out validation set of generated WMDP-like questions, we recorded the final-token representation from each layer of the fine-tuned model during its forward pass. Specifically, for each prompt x , we collect:

$$\begin{aligned}\text{Act}_\ell^{(\text{locked})}(x) &= \text{Hidden}_\ell(x_{\text{locked}})[-1], \\ \text{Act}_\ell^{(\text{elicited})}(x) &= \text{Hidden}_\ell(x_{\text{elicited}})[-1],\end{aligned}$$

We then apply the global layer-wise topological analysis outlined in 3.2 to this representation data to study how the model’s latent space differs between *locked* (no password) and *elicited* (correct password) states.

C.4 Global PH pipeline and resource constraints

All Vietoris–Rips barcodes are computed with the GPU build of RIPSER++ on a single node equipped with four NVIDIA A100 GPUs (80 GB each). Per layer we draw $K = 128$ independent subsamples of $k = 4096$ activation vectors (64 clean, 64 adversarial). Subsamples are dispatched round-robin to two concurrent RIPSER++ kernels per GPU.

Memory footprint. A complete $k = 4096$ complex truncated at dimension 2 occupies only 2.1 ± 0.4 GB of device memory (95-th percentile < 2.8 GB; Tab. 6), leaving a wide margin inside the 80 GB budget, even when two barcodes are built concurrently on the same GPU.

Throughput. The mean wall-time per barcode is 36.8 ± 0.6 s (95-th percentile < 40 s). With four GPUs processing eight barcodes in parallel, a full layer (128 barcodes) finishes in ≈ 10 min and the five-layer suite of one model in ≈ 50 min. Running the six models serially therefore completes in about five hours on a single $4 \times$ A100 node—comfortably within the nightly maintenance window.

Table 6: Per-barcode wall-clock time and GPU-memory consumption ($k = 4096$, dimension ≤ 2). Statistics over $K = 64$ barcodes drawn from the LLAMA-3 8B activations.

Layer	time $\mu \pm \sigma$ [s] (p95)	memory $\mu \pm \sigma$ [GB]
1	38.34 ± 0.76 (39.6)	2.27 ± 0.34
8	36.79 ± 0.70 (38.0)	2.12 ± 0.39
16	36.68 ± 0.45 (37.4)	2.13 ± 0.30
24	36.63 ± 0.71 (38.1)	2.03 ± 0.33
32	36.62 ± 0.54 (37.4)	2.20 ± 0.344

After choosing $K = 64$, we recomputed the Monte-Carlo variance σ_f^2 from the raw, unscaled feature values. For 39 out of 41 statistics we found $\sigma_f < 0.10$, which would put the standard error $\text{SE} = \sigma_f / \sqrt{K}$ below $\Delta^*/2 = 0.025$ with only $K \leq 20$. The outlier features were those which aggregate counts—total persistence of H_0 and the raw count of H_1 bars—and need to be transformed for their variance to be directly comparable to the other features. These do not affect the classifier as the features are scaled prior to training and also do not appear as the most informative features for distinguishing between clean and poisoned PH-derived features. We conservatively choose $K = 128$ and the resulting ROC-AUCs on the logistic regression model trained only on barcodes are perfect (1.00 ± 0.00), confirming that the subsampling budget is more than sufficient to validate the significance of the features derived from PH, while balancing GPU memory and computation time.